Fermi National Accelerator Laboratory

FERMILAB-Conf-94/275-E

Physics at the Fermilab Tevatron Proton-Antiproton Collider

Steve Geer

Fermi National Accelerator Laboratory
P.O. Box 500, Batavia, Illinois 60510

August 1994

Lectures given at the *Fifth BCSPIN Summer School in Physics,*
Kathmandu, Nepal, May 22- June 7, 1994

Operated by Universities Research Association Inc. under Contract No. DE-AC02-76CHO3000 with the United States Department of Energy

Disclaimer

CDF/PUB/CDF/PUBLIC/2787
FERMILAB-CONF-94/275-E

Physics at the Fermilab Tevatron Proton-Antiproton Collider

Steve Geer

Fermi National Accelerator Laboratory
P.O. Box 500, Batavia, Illinois 60510

Abstract

These lectures discuss a selection of QCD and Electroweak results from the CDF and D0 experiments at the Fermilab Tevatron Proton-Antiproton Collider. Results are presently based on data samples of about 20 pb^{-1} at a center-of-mass energy of 1.8 TeV. Results discussed include jet production, direct photon production, W mass and width measurements, the triboson coupling, and most exciting of all, evidence for top quark production.

Lectures given at the Fifth BCSPIN Summer School in Physics,
Kathmandu, Nepal; May 1994.

1 Introduction

In 1987 the Fermilab Tevatron Proton-Antiproton Collider began operation, and the Collider Detector at Fermilab (CDF) recorded its first data. The energy frontier had moved from the Sp$\bar{p}$S Collider at CERN ($\sqrt{s}$ = 630 GeV) to the Tevatron Collider at Fermilab ($\sqrt{s}$ = 1.8 TeV). Seven years later, in 1994, the Tevatron Collider is in the middle of its third major data taking run. The Collider physics program not only includes the exciting prospect of confirming the first evidence for top quark production and studying the properties of this very heavy fundamental particle, but also includes the precision electroweak measurement of the W mass, improved measurements of the W width, the three-boson couplings, a great variety of unique QCD tests, a rich program of b-quark physics, and the search for new phenomenon at the highest collision energies available in the laboratory. These lectures discuss some of the highlights from this very diverse and certainly exciting physics program.

1.1 A Brief Prelude

The 1987 CDF data sample was modest by todays standards, corresponding to an integrated luminosity of only 25 nb^{-1}. However, this initial data enable CDF to measure the basic characteristics of minimum bias events, jet production, and W$^{\pm}$ production at $\sqrt{s}$ = 1.8 TeV. During the second Tevatron collider run (1988-89) the CDF experiment recorded a more substantial data sample of 4 pb^{-1}. This large increase in integrated luminosity (more than two orders of magnitude) enabled corresponding improvements in the scope and precision of the CDF physics results. In particular, analysis of the 1988-89 CDF data yielded (i) measurements of the $W^{\pm}$ and Z^0 boson masses with precisions of 390 MeV/c^2 and 360 MeV/c^2 respectively, (ii) a measurement of the width of the $W^{\pm}$ bosons with a precision of 200 MeV, (iii) a search for the top quark and a lower limit of 91 GeV/c^2 on the top quark mass, (iv) measurements of Drell-Yan production and of the $W^{\pm}$ and Z^0 cross-sections, transverse momentum distributions, lepton asymmetries, and W + jet associated production, (v) measurements of B^0-$\overline{B^0}$ mixing, b quark production cross-sections, and the observation of several exclusive final states from B meson decay, (vi) comparisons with next-to-leading order perturbative QCD predictions of the inclusive jet and photon cross-sections, diphoton cross-section, jet shapes, dijet mass and angular distributions, and the photon angular distribution, (vii) comparisons with leading order perturbative QCD predictions of three-jet and four-jet rates and properties, and high total-transverse energy event rates and properties, and (viii)

search for new particles, including a light Higgs boson, additional heavy W-like and Z-like bosons, supersymmetric squarks and gluinos, and massive stable charged particles. The physics results from the 1988-89 run not only improved measurements of standard model parameters and limits on non-standard or as yet undiscovered particles, but also provided a glimpse of the potential of further collider runs. In particular, the steadily advancing limits on the top quark mass were making significant inroads into the mass window indicated by the world's electroweak measurements, thus suggesting that discovery of the top quark was just around the corner.

1.2 The Present Run

The third Tevatron collider run began in 1992, and is on-going. This run is the first data taking run for the D0 detector. Furthermore the CDF detector has been substantially upgraded. In particular the addition of a Silicon Vertex Detector at the center of CDF is yielding spectacular results. The excitement over the current collider run is based on expectations for a factor of about 30 - 40 times the integrated luminosity of the 1988-89 data sample, together with greatly improved detector capabilities, and tremendous prospects for top-quark physics. The first half of the present run (run 1a, 1992-93) yielded data samples of 19 pb^{-1} and 15 pb^{-1} for CDF and D0 respectively, which together represent almost an order of magnitude more data than previously recorded by CDF. There is already a long list of CDF and D0 physics results being presented at conferences. Some of these results are described in sections 5, 6, and 7. The most exciting result is undoubtedly the possible first observation of the top quark by CDF.

The end of the second part of run 1 (run 1b) is expected to occur in about one year from now. If all goes as planned, the experiments will have quadrupled their run 1a data samples. This should be enough to confirm or otherwise the observation of the top quark, and will hopefully be enough to begin to measure its production properties in addition to its mass. We can hope that studying this very heavy elementary particle will provide clues to the origin of particle masses. In addition to the excellent prospects for the top quark, the steady improvement in W mass measurements and the study of the three-boson couplings are expected to yield interesting electroweak results from the run 1 data. QCD tests and b-quark studies are also expected to make significant progress, but perhaps the most exciting possibility is that of finding something completely new. With a factor of thirty to forty more data than in the

1988-89 run, we can always hope.

2 The Tevatron Proton Antiproton Collider

Making, accumulating, and colliding antiprotons requires a complex of accelerators and storage rings. At Fermilab this accelerator complex consists of:

- **LINAC**
  Linear accelerator that accelerates protons to 400 MeV.

- **BOOSTER**
  Proton Synchrotron that accelerates the LINAC protons from 400 MeV to 8 GeV.

- **MAIN RING**
  Proton Synchrotron that (i) accelerates approximately 10^{12} Booster protons per second from 8 GeV to 120 GeV for antiproton production, (ii) accelerates the Booster protons to 150 GeV for injection into the Tevatron collider, and (iii) accelerates 8.9 GeV antiprotons from the Accumulator to 150 GeV for injection into the Tevatron collider.

- **TARGET STATION**
  Antiproton production target plus Lithium Lens. The target assembly consists of a stack of Ni, Cu, Al, and powdered Rhenium. The main ring delivers $O(10^{12})$ protons per pulse onto the target, and roughly one in every 10^5 proton interactions produces an antiproton. Downstream of the target, a Lithium lens focuses 8.9 GeV/c negative particles to a 4.2 mm spot for transfer into the Antiproton Debuncher.

- **DEBUNCHER**
  Storage ring that collects negative particles within a 60 mrad cone. The debuncher has a 200 ns orbit length. Thus pions and muons decay within a few turns, leaving only antiprotons. The incoming RF bunch structure is removed before the antiprotons are transferred to the accumulator.

- **ACCUMULATOR**
  Storage Ring in which antiprotons are accumulated for many hours and stored at 8.9 GeV/c in a 474m circumference orbit. The beam lifetime is typically 300 hours. The beam is cooled stochastically. The incoming $\Delta P/P = 0.2\%$ is reduced to 0.05%.

- TEVATRON COLLIDER

  Accelerates protons and antiprotons circulating in opposite directions from the injection energy of 150 GeV up to the colliding beam energy of 900 GeV, and stores the beams in colliding mode for many hours. The circumference of the collider is 6.28 Km, which accommodates 774 superconducting 4.4 Tesla dipoles, and 216 quadrupoles.

3 The CDF Detector

CDF is a general-purpose detector designed to study the physics of $p\bar{p}$ collisions. A side-view cross section of CDF is shown in Fig. 1. The polar angle (θ) in spherical coordinates is measured from the proton beam axis, and the azimuthal angle (ϕ), from the plane of the Tevatron. A 4.8 m long superconducting solenoid of radius 1.5 m generates a 1.4 Tesla magnetic field. Tracking chambers inside the field volume are used to detect charged particles and measure their momenta. Surrounding the solenoid are sampling calorimeters used to measure the electromagnetic and hadronic energy of jets and electrons. Outside the calorimeters are drift chambers used for muon detection.

The solenoid and tracking volume of CDF is surrounded by calorimeters which cover 2π in azimuth, and in pseudorapidity, η, from -4.2 to 4.2, where $\eta = -\ln(\tan(\theta/2))$. The calorimeters are segmented in ϕ and η to form a projective tower geometry which points back to the interaction point. There are three separate η regions; the central, end-plug, and forward. Each region has an electromagnetic calorimeter (CEM,PEM,FEM) and behind it an hadronic calorimeter (CHA/WHA,PHA,FHA). In all cases, the absorber in the hadronic calorimeter is iron, and in the electromagnetic calorimeter, lead. The coverage, thickness and resolutions of the calorimeters are summarized in Table 1. The energy resolution is given as a function of E_T , the projection of the observed energy (E) onto the plane transverse to the beam axis ($E_T = \mathrm{E}\sin\theta$). The central towers are 15° wide in ϕ and 0.1 units wide in η, and use scintillator as the active sampling medium. Located six radiation lengths deep in the CEM calorimeter, approximately at shower maximum for electromagnetic showers, are the central proportional chambers with strip and wire readout (CES). The CES provides shower-position measurements in both the z and $r-\phi$ views. Proportional chambers located between the solenoid and the CEM (CPR) sample the early development of electromagnetic showers in the material of the solenoid coil. In the end-plug and forward region, gas proportional chambers are used as the active media in the calorimeters and the tower size is 5° in ϕ, and

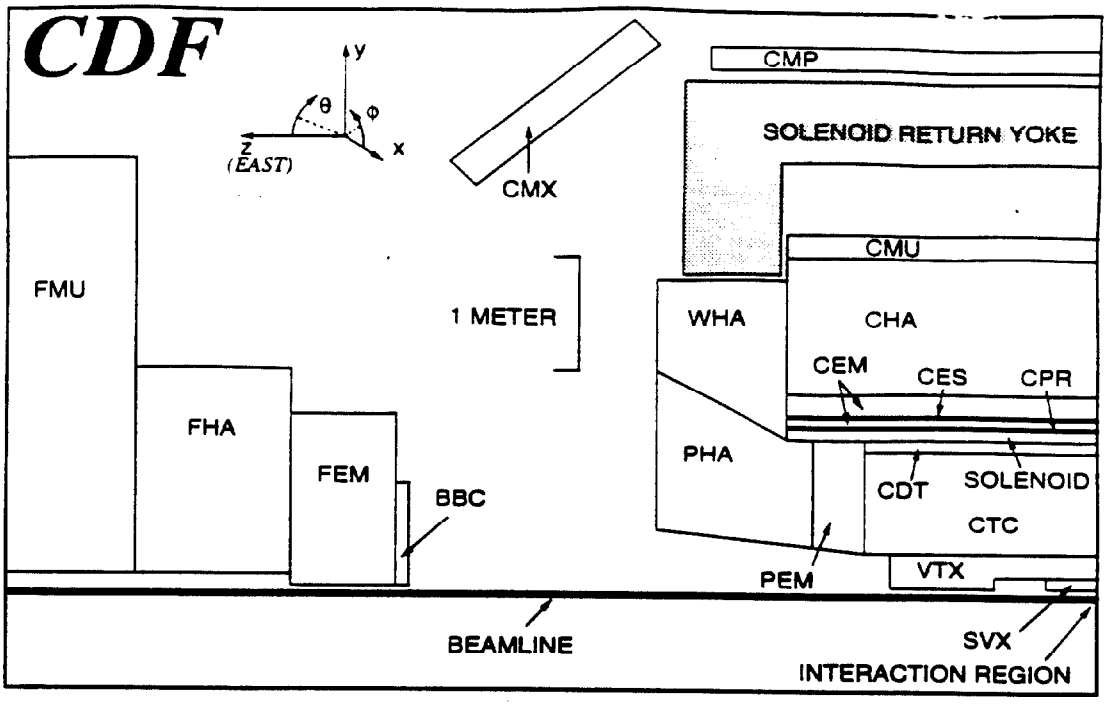

Figure 1: A side-view cross section of the CDF detector. The detector is forward-backward symmetric about the interaction region, which is at the lower-right corner of the figure. See text for detector component definitions.

0.1 units in η.

Within the magnetic field of the solenoid are three tracking chambers for charged particles. Surrounding the 1.9 cm radius beryllium beampipe is a 4 layer silicon microstrip vertex detector (SVX), which was installed in CDF in 1992. The SVX is 51 cm long and consists of two identical cylindrical modules which meet at $z = 0$. Because $p\bar{p}$ interactions are spread along the beamline with standard deviation $\sigma \sim 30$ cm, the geometrical acceptance of the SVX is about 60% for $p\bar{p}$ interactions. The four layers of the SVX are at distances of 3.0, 4.2, 5.7 and 7.9 cm from the beamline. Axial microstrips with 60 μm pitch on the three innermost layers and 55 μm pitch on the outermost layer provide precision track reconstruction in the plane transverse to the beam. The SVX single-hit and impact parameter resolutions are measured to be $\sigma = 13$ μm and $\sigma = 17$ μm respectively.

Outside the SVX, a vertex drift chamber (VTX) provides tracking information up to a radius of 22 cm and $|\eta|$ <3.25. The VTX is used to measure the $p\bar{p}$ interaction vertex along the z axis with a resolution of 1 mm. Both the SVX and VTX are mounted inside the central tracking chamber (CTC), which is a 3.2m-long drift chamber with an outer radius of 132 cm containing 84 concentric, cylindrical layers of sense wires. Sixty layers have wires parallel to the beam direction (axial wires) and provide tracking in the $r - \phi$ plane. Twenty-four layers (stereo) are tilted at +3° or -3° with respect to the beam direction. Together, the

System	η Range	Energy Resolution	Thickness
CEM	$\lvert\eta\rvert < 1.1$	$13.7\%/\sqrt{E_T} \oplus 2\%$	18 X_0
PEM	$1.1 < \lvert\eta\rvert < 2.4$	$22\%/\sqrt{E} \oplus 2\%$	18-21 X_0
FEM	$2.2 < \lvert\eta\rvert < 4.2$	$26\%/\sqrt{E} \oplus 2\%$	25 X_0
CHA	$\lvert\eta\rvert < 0.9$	$50\%/\sqrt{E_T} \oplus 3\%$	4.5 λ_0
WHA	$0.7 < \lvert\eta\rvert < 1.3$	$75\%/\sqrt{E} \oplus 4\%$	4.5 λ_0
PHA	$1.3 < \lvert\eta\rvert < 2.4$	$106\%/\sqrt{E} \oplus 6\%$	5.7 λ_0
FHA	$2.4 < \lvert\eta\rvert < 4.2$	$137\%/\sqrt{E} \oplus 3\%$	7.7 λ_0

Table 1: CDF calorimeter properties. The symbol $\oplus$ signifies addition in quadrature. Energy resolutions for electromagnetic calorimeters are for incident electrons and photons, and for hadronic calorimeters are for incident pions. Energy is in GeV. Thicknesses are in radiation lengths (X_0) and interaction lengths (λ_0).

axial and stereo wires provide tracking in the $r-z$ plane. The momentum resolution of the SVX/CTC system is $\frac{\delta P_t}{P_t} = [(0.0009P_t)^2 + (0.0066)^2]^{\frac{1}{2}}$, where p_T has units of GeV/c.
The central calorimeters act as a hadron absorber for the central muon detection system (CMU), which consists of four layers of drift chambers located outside the central hadronic calorimeter. The CMU covers $|\eta| < 0.6$ and can be reached by muons with p_T in excess of 1.4 GeV/c. In 1992, 0.6 m of steel was added behind the CMU for additional hadron absorption, and an additional four layers of drift chambers were added behind the steel to detect muons. This system is referred to as the central muon upgrade (CMP). Approximately 84% of the solid angle for $|\eta| < 0.6$ is covered by CMU, 63% by CMP and 53% by both. In addition, the coverage of the central muon system has been extended to cover the range $0.6 < |\eta| < 1.0$ through the addition of four conical arches which hold drift chambers for muon detection, sandwiched between scintillator counters for triggering. This system is called the central muon extension (CMX). Approximately 71% of the solid angle for $0.6 < |\eta| < 1.0$ is covered by CMX. In all muon systems in the central region, muon p_T is measured with charged tracking and has a tracking resolution as discussed above.

4 The D0 Detector

The D0 detector design stresses uniform, hermetic, fine-grained calorimetry, large solid angle coverage and excellent muon detection. The Detector (Fig. 2) includes three major components: the outer Muon System, the inner Central Tracking System, and the liquid argon Calorimeter System.
The Muon System consists of five iron toroids, 1.1–1.5 meters thick, and three layers of

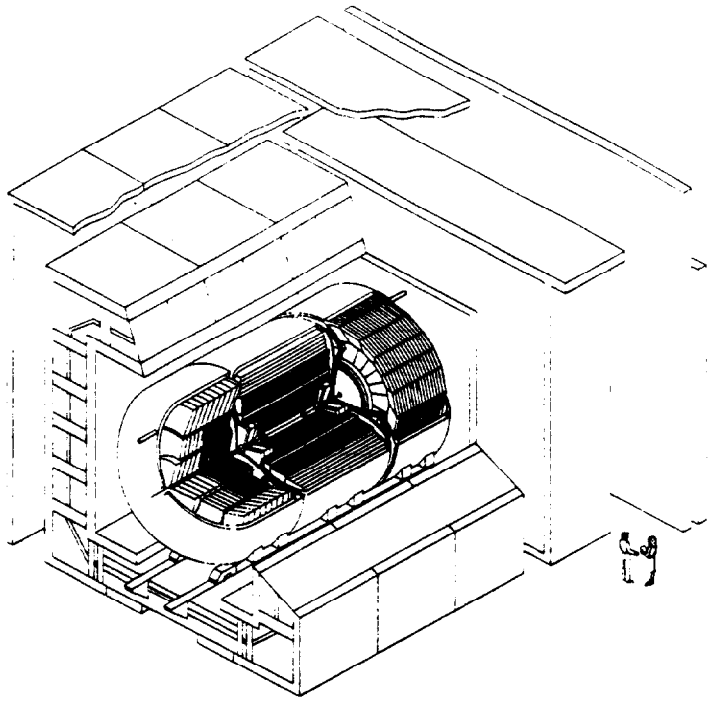

Figure 2: The DØ Detector

proportional drift tube (PDT) chambers. The central toroid surrounds the calorimeter and covers angles down to 45°. The end toroids and the small angle muon system cover the forward region down to 5°. Thus there is full muon coverage for $| \eta | \leq 3.2$. The momentum of a muon is determined by using the PDT chambers to measure the deflection of the muon trajectory in the 1.9 T steel toroids. The momentum resolution, typically 20%, is dominated by multiple scattering for momenta < 80 GeV/c. The combined calorimeter plus toroid thickness varies from 14 λ in the central region to 19 λ in the end regions. This thickness reduces backgrounds from hadronic punchthrough to a negligible level.

The Central Tracking System (Fig. 3) consists of four main components: Vertex Chamber, Transition Radiation Detector, Central Drift Chamber and two sets of Forward Drift Chambers. The Vertex Chamber has three cylindrical layers of jet-type cells, and every cell in a layer has eight sense wires. It provides precision charged particle tracking with good azimuthal spatial resolution (60 μm) and good two-track resolution (0.6 mm). Charge division is used to measure the axial coordinate with a resolution of about 1 cm. The chamber is also used to find secondary vertices, and reject photon conversions which can give a fake electron signal. The Transition Radiation Detector provides additional rejection of pions in the identification of central electrons. It has three cylindrical layers, each layer consisting of a set of polypropylene foils surrounded by a radial drift X-ray detector. A pion rejection

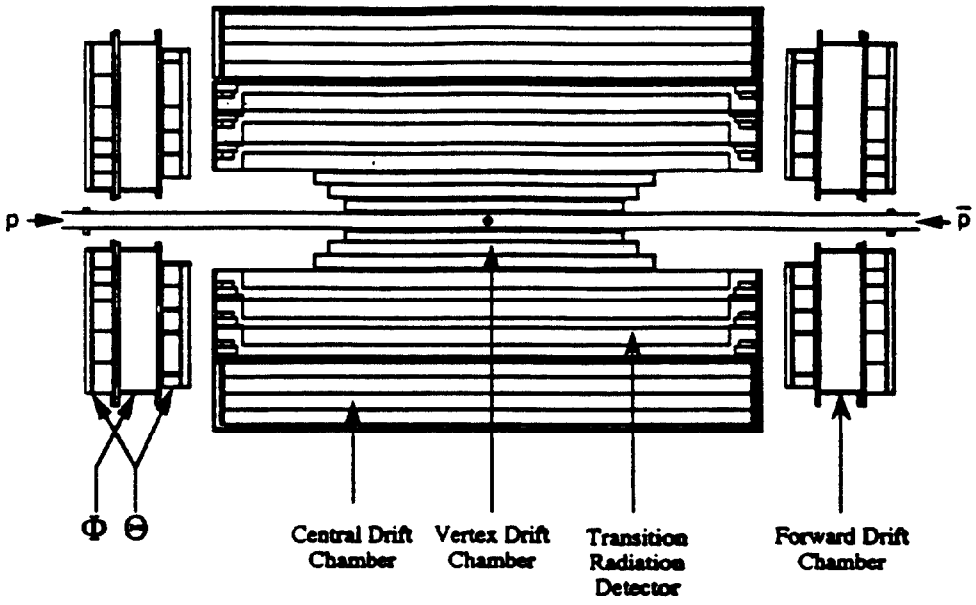

Figure 3: The DØ Central Tracking System.

factor of 50 was achieved in a test beam for an electron efficiency of 90%. The Central Drift Chamber has four cylindrical layers of jet-type cells, and every cell in a layer has seven sense wires. Its azimuthal spatial resolution is 150 μm. The axial position of tracks is measured with delay lines, with a resolution of 4 mm. Measurements of dE/dx are used to help identify conversions. The Forward Drift Chambers cover angles down to 5°, and include two types of units. The Φ units have radial sense wires, with 16 measurements along each track. The Θ units have sense wires oriented transversely to the beam, with 8 measurements along each track in each of the two units. The spatial resolution in each unit is 200 μm.

The DØ calorimeters are sampling calorimeters using uranium as the absorbing material and liquid argon as the sampling medium. The use of uranium not only leads to a compact calorimeter design, but it helps in equalizing the calorimeter response to electrons and hadrons. This is important for minimizing the fluctuations in the observed energies of jets, whose particle content may vary. Liquid argon is used as the active ionization medium because of its ease of calibration, its stability and uniformity of response, and its radiation hardness. The DØ Calorimeter System consists of a cylindrical Central Calorimeter and two End Calorimeters covering angles down to within 1° of the beamline. Each of the three

calorimeters contains an electromagnetic section with thin uranium plates, a fine hadronic section with thick uranium plates, and a coarse hadronic section with very thick copper or steel plates. Printed circuit boards with segmented detection pads are interleaved between the absorber plates to detect the ionization in the liquid argon. All of the DØ calorimeter modules use a uniform technology to facilitate the relative calibration between modules. The calorimeters are designed with minimal cracks and other uninstrumented regions in order to provide essentially hermetic coverage. The calorimeters are finely segmented both longitudinally and transversely. Longitudinally, each electromagnetic section is divided into 4 readout depths (for a total of 21 X_o), and the hadronic sections are divided into 4–5 depths (for a total of 7–9 λ). The transverse segmentation is 0.1 × 0.1 for $\Delta\eta \times \Delta\phi$, except in the third electromagnetic longitudinal section (where shower maximum occurs), where the segmentation is increased to 0.05 × 0.05 for better shower position resolution. The readout cells are arranged in semi-projective towers. Typical electromagnetic and hadronic calorimeter modules have been extensively tested with electrons and pions from 2 to 150 GeV in a test beam at FNAL. The fractional energy resolution of electrons in the calorimeters is $15\%/\sqrt{E}$, and of pions is $50\%/\sqrt{E}$. The spatial position resolution for electrons is 1–2 mm, for energies above 50 GeV. Using the transverse and longitudinal shower shape information from the electromagnetic and hadronic modules, a pion rejection factor of greater than 1000 has been measured for a 95% electron efficiency. The e/π response of the calorimeter system is energy dependent but varies within the range 1.04–1.12 for energies between 10 and 100 GeV.

5 Testing Quantum Chromodynamics

In the first few years of high-energy proton-antiproton collider physics a large number of different hard-scattering processes with final state jets, photons, $W^{\pm}$ and Z^0 bosons were measured and the differential cross-sections confronted with the predictions of perturbative Quantum Chromodynamics (QCD). The main thrust of this effort was devoted to determining to what extent leading order (LO) matrix element calculations, and the predictions of parton shower Monte Carlo programs (LO plus gluon radiation) could describe the data. In general it was found that LO QCD calculations correctly predict these hard scattering differential cross-sections with a precision of typically ±50%. The dominant theoretical uncertainties on the LO predictions were associated with the choice of renormalization scale

and the uncertainty on the proton structure function. The main experimental uncertainties were statistical and, in processes having final state jets, the uncertainties associated with the jet energy scale. In the last few years (i) the statistical precision of the data has greatly improved, (ii) next-to-leading order (NLO) perturbative QCD predictions have become available for a number of processes, and (iii) there has been steady progress in our knowledge of the proton structure function. These improvements have resulted in more precise tests of perturbative QCD in hadron collisions. Although we cannot yet claim to be making precision (for example 1%) tests of QCD, we are certainly making progress in that direction. As an example, the inclusive jet cross-section has now been compared to the NLO QCD predictions with a precision of $\pm 20\%$.

5.1 Jets

Within the framework of Quantum Chromodynamics the proton and antiproton contain partons (quarks and gluons). A Proton-Antiproton Collider is therefore a parton-parton collider. Perturbative QCD calculations predict that occasionally a parton from the proton scatters from a parton from the antiproton. The two outgoing scattered partons hadronize to form jets of physical particles. If these hadron jets are sufficiently energetic and at sufficiently large angle with respect to the beam direction, then they can be detected and their energies and directions measured. In this case $2 \rightarrow 2$ scattering results in two hadronic jets in the final state whose momentum components balance in the plane transverse to the beam direction. Fig. 4 shows the so called "Lego" plot for a typical two-jet event observed in the CDF detector. The Lego plot shows the transverse energies measured in each calorimeter cell. The grid delineates the cell boundaries on the calorimeter surface, where the cylindrical calorimeter has been unwrapped to form a flat surface in (η,ϕ)-space. Notice that the two calorimeter clusters balance each other .. they have approximately equal transverse energies and are back-to-back in azimuthal angle. To reconstruct the energies and directions of jets observed in the detector we must use a jet algorithm. The details of the jet algorithm used depend on the detector (CDF or D0) and to some extent on the particular analysis being done. The CDF and D0 jet algorithms used for the results described in the following sections are approximately as follows. A cone is defined in (η, ϕ)-space, centered on the jet direction, and with radius $R = (\Delta\eta^2 + \Delta\phi^2)^{1/2}$. All calorimeter cells within the cone are associated to the jet, and the jet energy $E_J = \sum E_i$ where i runs over all associated cells. Typically, CDF

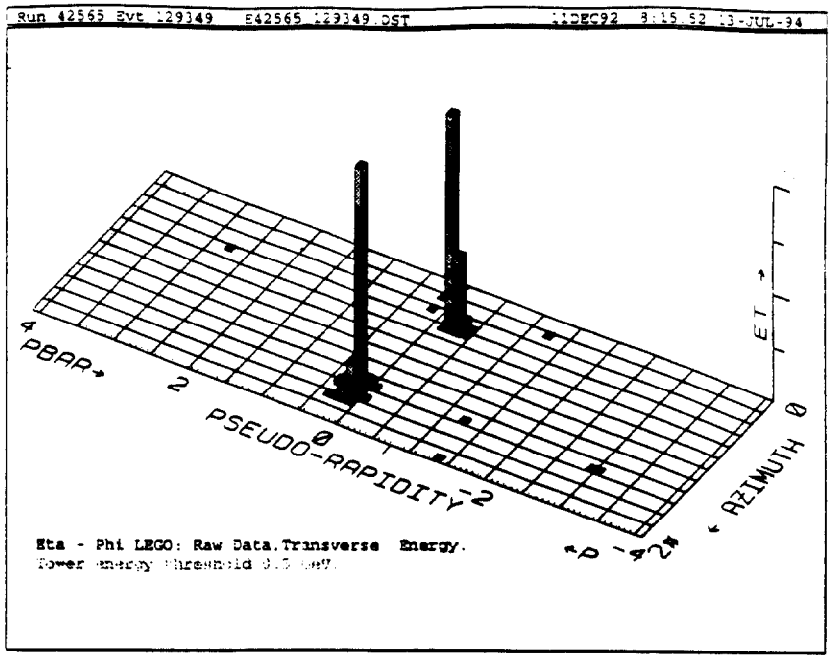

Figure 4: Lego plot for a spectacular two-jet event observed in the CDF detector.

jet analysis use a cone size R = 0.7 and D0 use a cone size R = 0.5.

5.2 The Jet Cross-Section and Quark Substructure

Within the framework of perturbative QCD the two-jet cross-section can be written:

$$\sigma(\overline{p}p \to cd) = \sum_{a,b} P(p \to a)\, P(\overline{p} \to b)\, \hat{\sigma}(ab \to cd) \tag{1}$$

where $P(p \to a)$ is the probability to find a parton of type a in the proton, $P(\overline{p} \to b)$ is the probability to find a parton of type b in the antiproton, and the $\hat{\sigma}(ab \to cd)$ are the parton-parton subprocess cross-sections.

More explicitly, the differential cross-section can be written in terms of the parton-parton center-of-mass scattering angle (θ^*), the incoming parton momentum fractions (x_a and x_b), and the four-momentum-transfer squared (Q^2):

$$\frac{d^3\sigma}{dx_a dx_b d\cos\theta^*} = \sum_{a,b} \frac{F_p(x_a, Q^2)}{x_a} \frac{F_{\overline{p}}(x_b, Q^2)}{x_b} \frac{d\hat{\sigma}_{ab}}{d\cos\theta^*} \tag{2}$$

where the $F(x, Q^2)/x$ are the structure functions that parameterize the parton densities inside the proton and antiproton. Perturbative QCD tells us how the structure functions evolve with Q^2. Hence, measurements of parton densities made in deep inelastic scattering experiments at relatively low Q^2 can be used to predict the parton distributions at the higher

values of Q^2 relevant to jet physics at collider energies. The subprocess differential cross-sections $\mathrm{d}\hat{\sigma}_{ab}/\mathrm{d}\cos\theta^*$ can be calculated within the framework of perturbative QCD. Hence, armed with knowledge of the structure functions and the calculated subprocess cross-sections, the triply differential two-jet cross-section can be calculated, or the necessary integrations can be done to predict differential or doubly differential two-jet or inclusive jet cross-sections. We begin with the CDF and D0 inclusive jet differential cross-sections $d\sigma/\mathrm{d}E_T$, which are shown in Figures 5, 6, and 7. The jet E_T distributions extend out to transverse energies approaching 500 GeV, and are well described by both LO [$\mathrm{O}(\alpha_s^2)$] and NLO [$\mathrm{O}(\alpha_s^3)$] predictions, over a range in which the jet rate falls by ten orders of magnitude. The similarity of the LO and NLO predictions shows that the NLO corrections to the LO predictions are small, which suggests that the perturbation series is under control (α_s small), and the predictions are reliable. Figure 6 compares the CDF measurements with the QCD predictions on a linear scale ([Data-Theory]/Theory). Note that the dependence of the predictions on the choice of renormalization scale shrinks from more than $\pm 20\%$ at LO to about $\pm 5\%$ at NLO, which increases our confidence that the perturbation series is rapidly converging. The dominant remaining theoretical uncertainty at NLO arises from the uncertainty on the structure functions, and is $\pm 20\%$.

The agreement between the measured and predicted $d\sigma/\mathrm{d}E_T$ distributions can be used to place a limit on quark substructure. To do this we need a definite model which describes how the measured distribution would be modified. The model commonly used is that of Eichten et al. (PRL 50, 811 (1983)) which introduces a contact term that switches on at a scale Λ_c:

$$L_{qq} = \pm\frac{g^2}{2\Lambda_c}\bar{q}_L\gamma_\mu q_L\bar{q}_L\gamma^\mu q_L \tag{3}$$

As Q^2 approaches the substructure scale the contact interaction results in an excess of large angle scatters (c.f. Rutherford scattering) which would tend to flatten the jet spectrum at large E_T. The absence of any evidence for this flattening (Fig. 5) has enabled CDF to place the limit of:

$$\Lambda_c > 1.45\ TeV\ \ (90\%\ C.L.) \tag{4}$$

which corresponds to a substructure distance scale $R_c < 1.4 \times 10^{-17}$ cm.

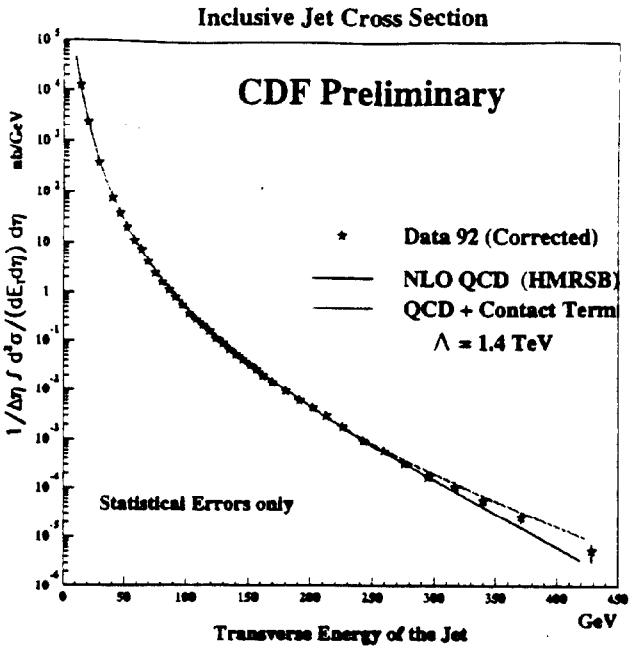

Figure 5: CDF inclusive jet differential cross-section compared with NLO QCD predictions and expectations for QCD modified by a contact term (see text).

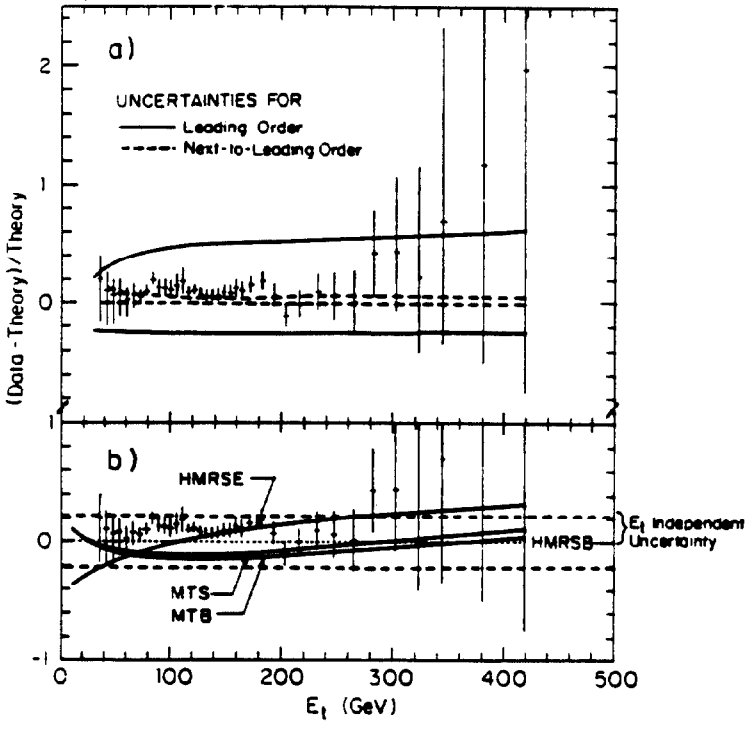

Figure 6: CDF inclusive jet differential cross-section compared with LO and NLO QCD predictions shown on a linear scale for (a) different renormalization scale choices, and (b) different structure function parameterizations.

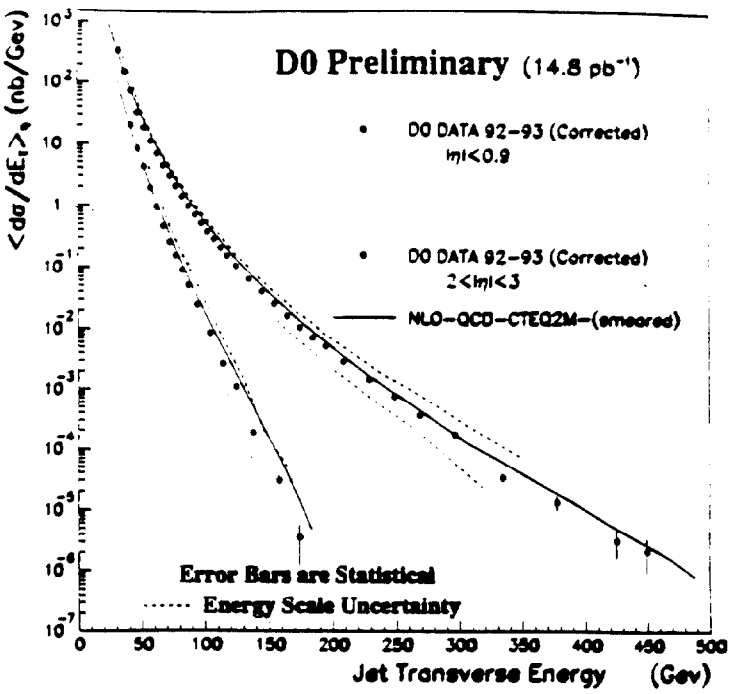

Figure 7: D0 inclusive jet differential cross-section compared with NLO QCD predictions

5.3 Two-Jet Physics

In its rest-frame, a system of two massless final state partons can be be fully specified by two parameters, which are conveniently taken to be the final-state mass $\sqrt{\hat{s}}$ and the center-of-mass scattering angle θ^*. It is therefore interesting to compare measured two-jet mass- and angular-distributions with QCD predictions.

The observed two-jet mass distribution from the CDF experiment is shown in Fig. 8 for events with two central jets ($|\eta| < 0.7$). The distribution extends out to masses of about 1 TeV, and is well described by both the LO and NLO predictions. There is no evidence for any deviations from the expected QCD behaviour.

In practice all of the LO subprocesses have angular distributions that are similar (but not identical) to the Rutherford scattering form (Fig. 9):

$$\frac{d\hat{\sigma}_{ab}}{d\cos\theta^*} \sim \frac{\alpha_s^2(Q^2)}{\hat{s}} (1 - \cos\theta^*)^{-2} \tag{5}$$

This single effective subprocess approximation to the LO prediction reflects the dominance of single gluon exchange diagrams at LO. The resulting two-jet angular distribution is therefore expected to have an approximate $(1 - \cos\theta^*)^{-2}$ dependence, although deviations from this naive expectation are expected to arise from scale-breaking effects since both $\alpha_s(Q^2)$ and F(x,Q^2) evolve with Q^2. Figure 10 shows that the measured two-jet angular distribution from

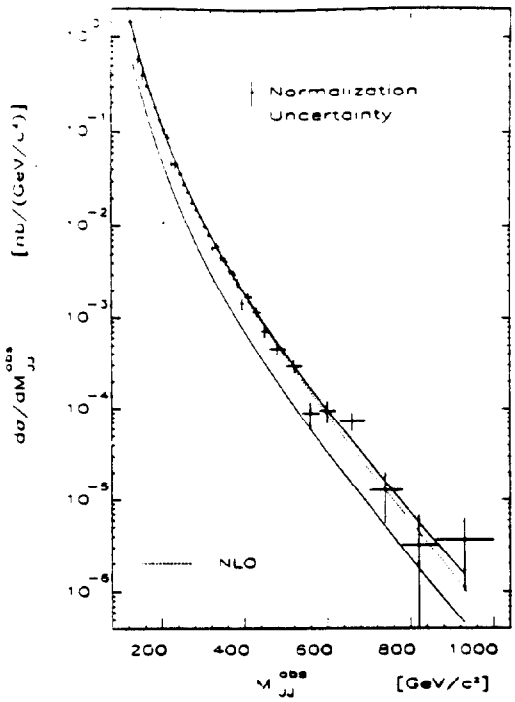

Figure 8: CDF two-jet mass distribution.

the D0 experiment is in excellent agreement with the LO QCD prediction. The anticipated scale breaking effects are evident. It is useful to define the angular variable :

$$\chi \equiv \frac{1+\cos\theta^*}{1-\cos\theta^*} = \frac{\hat{u}}{\hat{t}}. \tag{6}$$

Note that $\chi = 1$ for 90° scattering. When expressed in terms of χ the Rutherford scattering angular distribution is flat for $\chi \geq 2$. The angular dependence of the parton-parton

Parton Subprocess	$f_i(\chi)$
$q_1 q_1 \to q_1 q_1$	$\frac{8}{9}\left[F(\chi) - \frac{1}{3}(\chi + 2 + \chi^{-1})\right]$
$q_1 \overline{q_1} \to q_1 \overline{q_1}$	$\frac{8}{9}\left[F(\chi) + \frac{1}{3}(\chi - 1 + \chi^{-1}) + \frac{\chi^2+1}{(\chi+1)^2}\right]$
$qg \to qg$	$2\left[F(\chi) + \frac{4}{9}\left(\frac{1}{2}\chi + \frac{3}{2} + \frac{1}{2}\chi^{-1}\right)\right]$
$gg \to gg$	$\frac{9}{2}\left[F(\chi) + 2 - \frac{\chi}{(1+\chi)^2}\right]$

Table 2: Angular dependence of leading order QCD subprocess cross-sections.

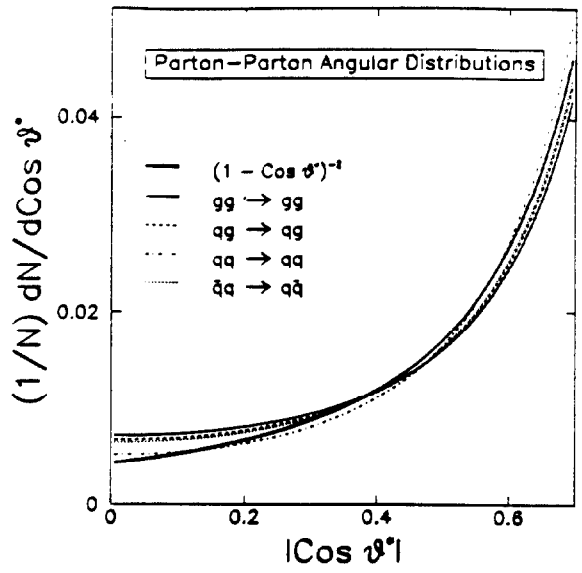

Figure 9: Calculated subprocess angular distributions for quark-antiquark, quark-gluon, and gluon-gluon scattering. The solid curve shows the expectation for Rutherford Scattering.

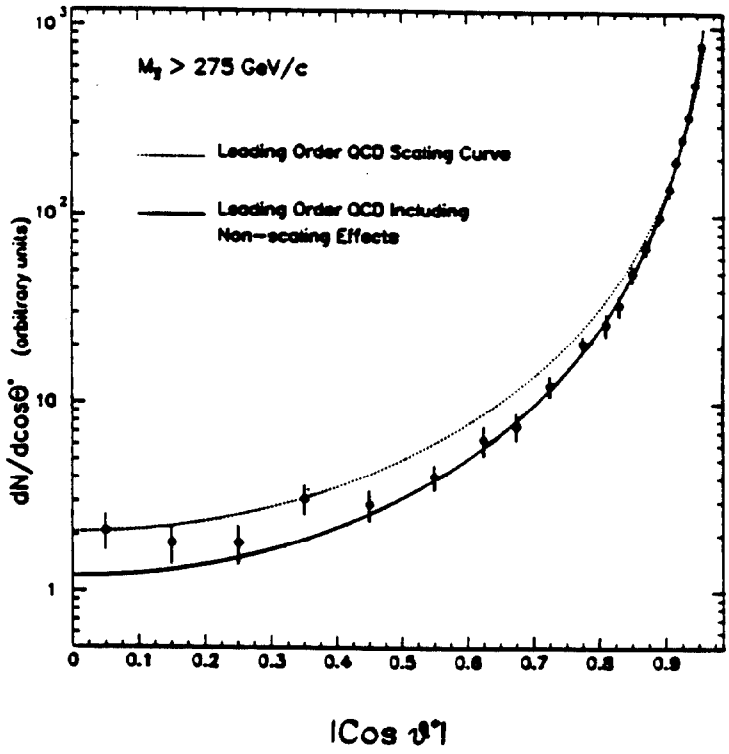

Figure 10: D0 two-jet angular distribution.

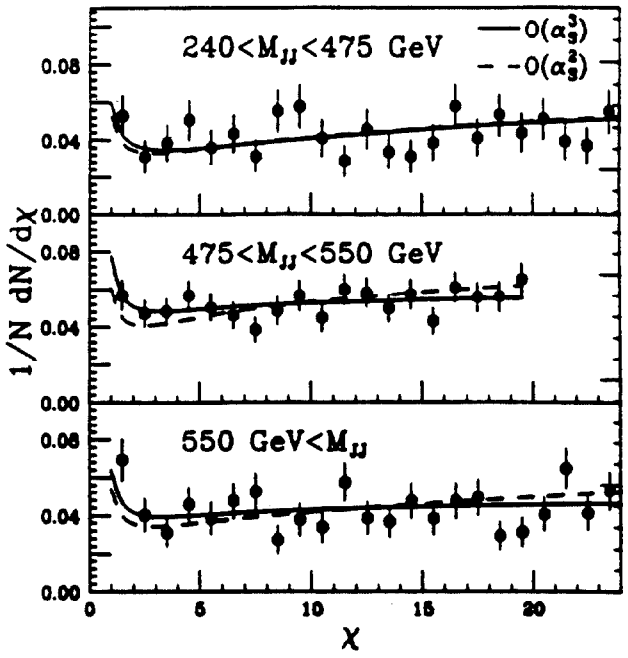

Figure 11: CDF two-jet angular distribution.

scattering matrix elements is given approximately by :

$$\frac{d\sigma}{d\chi} \sim \frac{F(\chi)}{(1+\chi)^2}, \tag{7}$$

where

$$F(\chi) \equiv \chi^2 + \chi + 1 + \frac{1}{\chi} + \frac{1}{\chi^2}. \tag{8}$$

More precisely, the exact form of the matrix element depends on the parton-parton subprocesses. The angular dependences for the various subprocesses i are given by:

$$\frac{d\sigma}{d\chi} \sim \frac{f_i(\chi)}{(1+\chi)^2} \tag{9}$$

or

$$\frac{d\sigma}{d\cos\theta^*} \sim \frac{f_i(\chi)}{(1+\chi)^2}\left[\frac{2}{(1-\cos\theta^*)^2}\right], \tag{10}$$

where $f_i(\chi)$ are listed in Table 2. CDF two-jet angular distributions $d\sigma/d\chi$ are compared with LO and NLO QCD predictions in Fig. 11. There is some evidence that the NLO predictions give a somewhat better description of the the observed distributions than the LO predictions. In these distributions the rise of $d\sigma/d\chi$ with increasing χ reflects the scale breaking effects expected in QCD. Note that at fixed mass, large χ corresponds to small Q^2.

5.4 Three-Jet Production

Higher order corrections to the basic $2 \rightarrow 2$ parton-parton scattering process can result in additional hard partons in the final state. At $O(\alpha_s^3)$, for example, there can be three-hard final-state partons which result in three-jet events. To completely describe a system of three massless final state partons in the three-body rest-frame, at fixed three-body mass we must specify four additional parameters. We therefore analyse three-jet events in a four-dimensional space. The normal convention is to label the incoming partons 1 and 2, and the outgoing final state partons 3, 4, and 5. The associated jets are ordered in decreasing center-of-mass energy such that $E_3 > E_4 > E_5$. We then choose the following four variables in the three-jet rest frame (see Fig. 12):

(i) $\cos\theta_3^*$, the cosine of the angle between the leading jet and the average beam direction (note that the incoming partons are not generally collinear in the three-jet rest frame).

(ii) ψ^*, the angle between the three-jet plane and the production plane (which contains the average beam direction and parton 3).

(iii) X_3, the energy fraction of the leading jet, where

$$X_i \equiv \frac{2\,E_i}{E_3 + E_4 + E_5} \tag{11}$$

Note that momentum conservation restricts X_3 to be in the range $2/3 < X_3 < 1$, and as $X_3 \rightarrow 1$ the three-jet system approaches a two-jet configuration.

(iv) X_4, the energy of the next-to-leading jet. Note that momentum conservation restricts X_4 to be in the range $1/2 < X_4 < 1$.

The beauty of this choice of variables is that the phase-space density is is uniform in $\cos\theta_3^*$, ψ^*, and also in the (X_3, X_4)-plane. Deviations from uniformity therefore tell us about the behaviour of the three-jet matrix element. Figure 13 compares QCD predictions with the observed distributions of X_3, X_4, $\cos\theta_3^*$, and ψ^* measured by the CDF collaboration in events with large total transverse energies. The predictions give an excellent description of the data. Note that in this analysis the requirement $X_3 < 0.9$, which is imposed to avoid experimental uncertainties when two jets get very close together, keeps events away from the two-jet pole. The D0 collaboration are also performing a three-jet analysis.

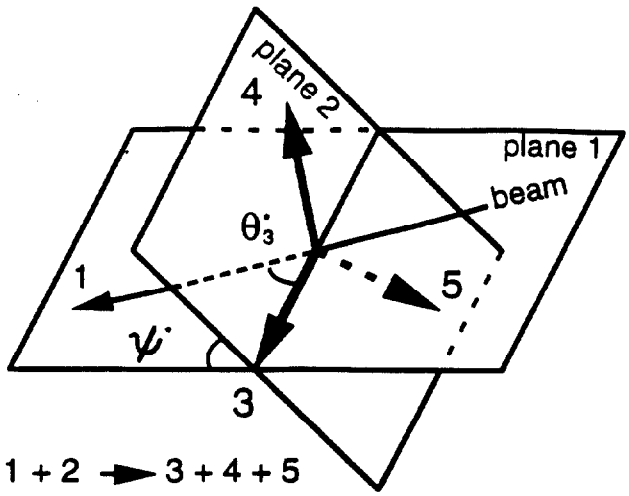

Figure 12: Three-Jet variables.

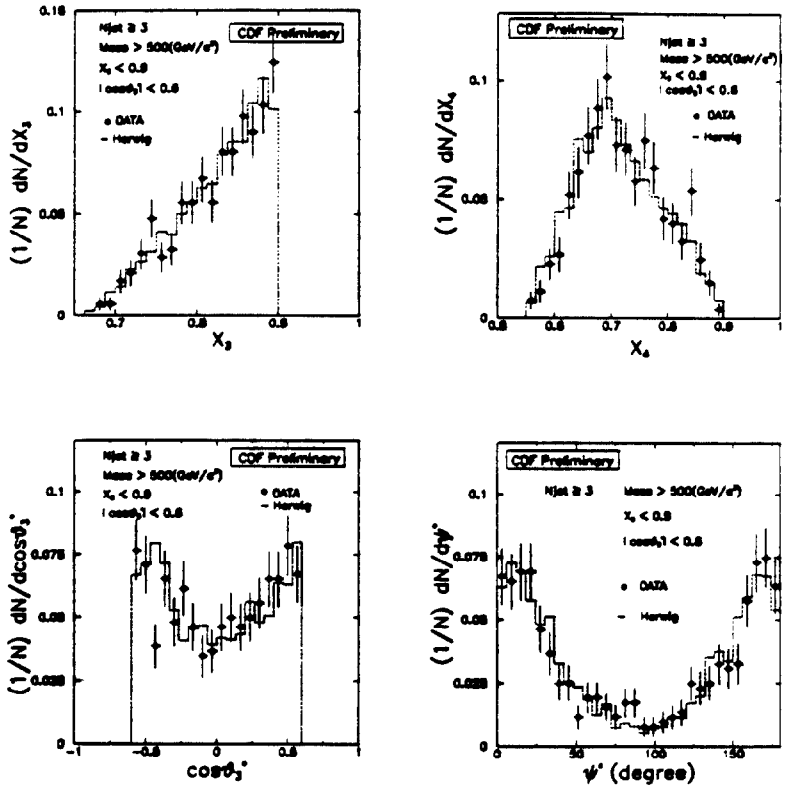

Figure 13: Three-jet variables. Comparison of observed distributions (points) of the three-jet variables (see text) with the HERWIG parton shower Monte Carlo predictions (Histograms) for events with total $E_T > 420$ GeV.

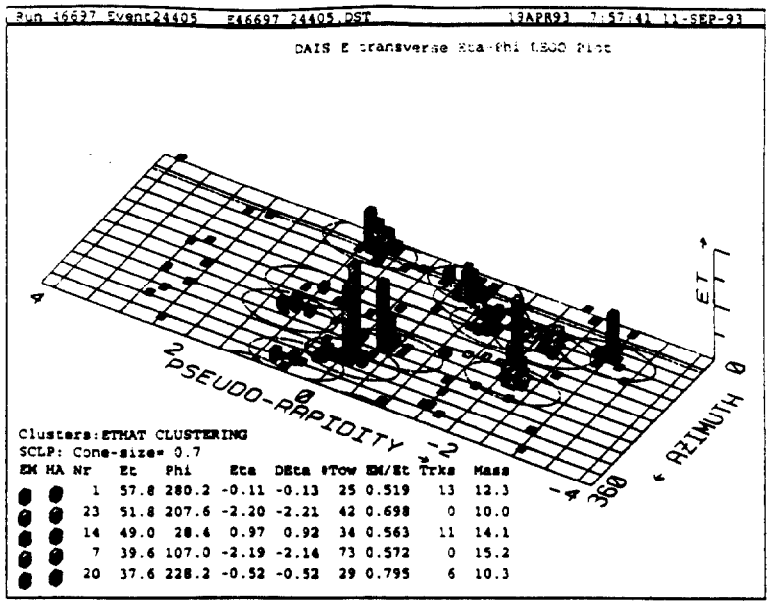

Figure 14: CDF event with ten final state jets having $E_T > 20$ GeV.

5.5 Multijet Production at High Total Transverse Energy

The Tevatron proton-antiproton collider produces collisions at the highest center-of-mass energies available in the laboratory. It is therefore of interest to look at the properties of the "hottest" events produced in these collisions. CDF have analysed a sample of events with total transverse energies:

$$\sum E_T > 420\ GeV \tag{12}$$

where the sum is over all jets with $E_T > 20$ GeV. These events can contain many jets. For example, the event with the largest number of reconstructed jets (Fig. 14) is a ten-jet event. Unfortunately, complete LO matrix element calculations are not available for topologies with more than 5 final state jets. Therefore, to compare with QCD expectations CDF uses the HERWIG parton shower Monte Carlo program, which can be thought of as the LO $2 \rightarrow 2$ matrix element plus gluon radiation. The HERWIG predictions for the jet multiplicity distributions are shown in Fig. 15 to give a reasonable description of the observed distribution for multiplicities of up to about 6 final state jets, but tend to underestimate the rate of events with larger jet multiplicities.

The HERWIG Monte Carlo program correctly predicts the two-, three-, four-, five-, and six-jet mass distributions (Fig. 16). Note that the exact LO matrix element predictions are also shown for topologies with up to five-jets, and these predictions are in agreement

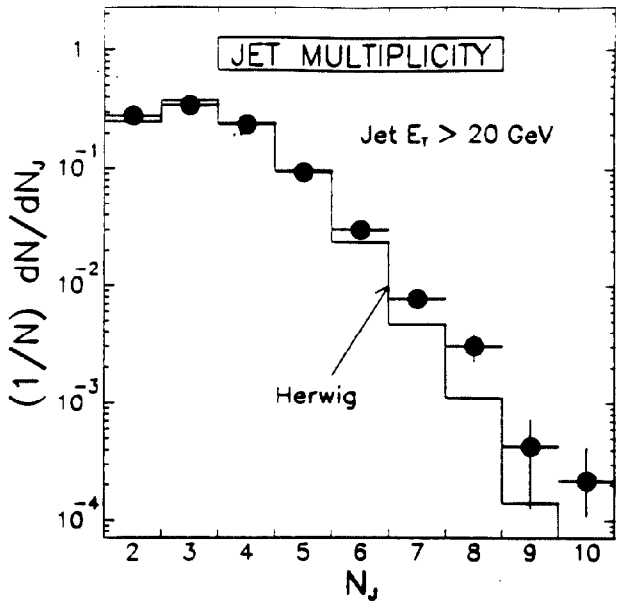

Figure 15: Preliminary Jet Multiplicity distribution (points) measured by CDF in events with total $E_T > 420$ GeV, compared with the HERWIG parton shower Monte Carlo prediction (Histogram)

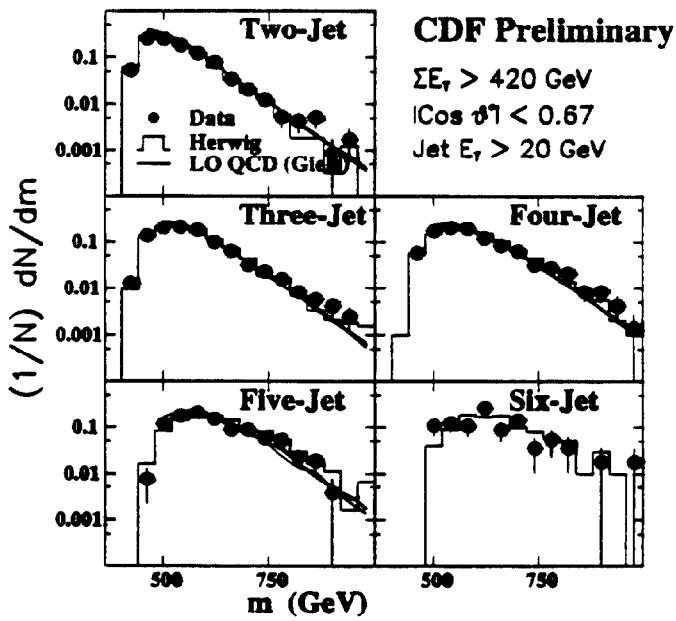

Figure 16: Multijet mass distributions. The data (solid points) are compared with HERWIG parton shower Monte Carlo predictions (Histograms), and complete LO QCD predictions (curves).

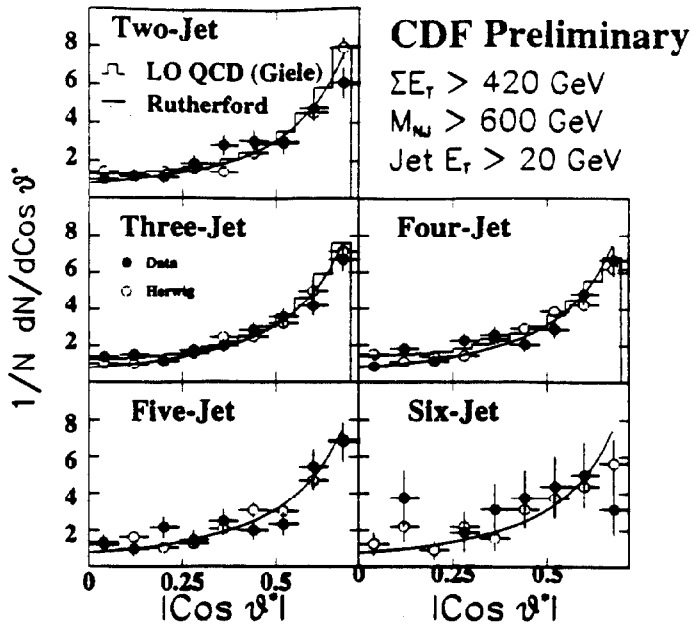

Figure 17: Leading jet angular distributions. The data (solid points) are compared with HERWIG parton shower Monte Carlo predictions (open points) for exclusive multijet final states. The histograms show LO QCD predictions. The curves show the expectation for Rutherford Scattering.

with the HERWIG predictions. It is interesting to note that all of the exclusive multijet mass distributions have similar shapes, falling exponentially above the turn-on. Finally, The leading jet angular distributions are compared with predictions in Fig. 17. All of these distributions are similar to the Rutherford scattering form. Thus it appears that multijet events at high $\sum E_t$ are well described by $2 \rightarrow 2$ scattering plus gluon radiation.

5.6 Direct Photon Physics and Excited Quarks

Since quarks carry electric charge they can radiate photons in quark-parton interactions. The dominant contribution to the LO predictions for production of these prompt photons comes from the Compton diagram ($qg \rightarrow q\gamma$). Prompt photons therefore probe the gluon distribution in the proton and antiproton, particularly at low x ($0.01 < x_T < 0.1$). NLO predictions are available for the prompt photon p_T distribution. Neither the measurements (which require a subtraction of background from jets that have fragmented to a leading π^0 or η) nor the NLO calculations (which require for example knowledge of the photon fragmentation function) are simple. The measured CDF and D0 prompt photon spectra

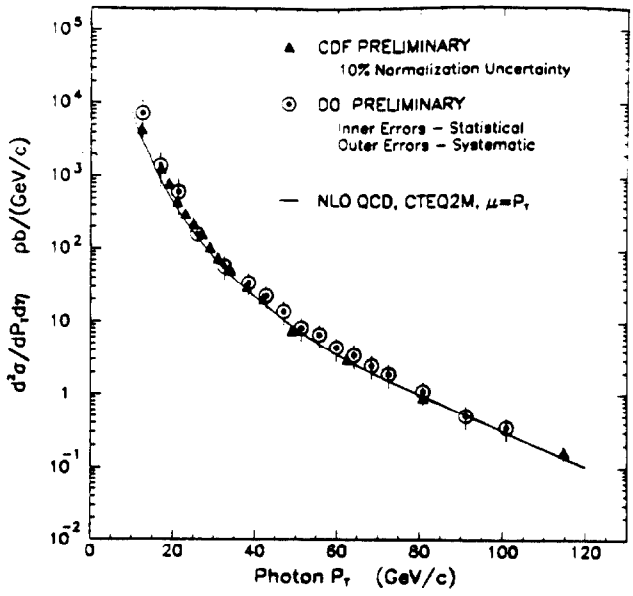

Figure 18: Direct photon spectrum.

are compared with the NLO prediction in Fig. 18. Of interest is the center-of-mass angular distribution of photons in photon+jet events. In contrast to two-jet events, where the dominant contributions come from spin-1 gluon exchange graphs, in the direct photon process, or in W + jet production, the dominant contributions come from spin-1/2 quark exchange graphs. We have seen in our previous discussion of two-jet physics that the spin-1 exchange process results in an approximate $(1 - \cos\theta^*)^{-2}$ angular dependence. We would expect the spin-1/2 exchange process to result in the less singular $(1 - \cos\theta^*)^{-1}$ angular dependence. In Fig. 19 we see that this is indeed observed to be the case, and that the QCD predictions give a reasonable description of all of these angular distributions.

Finally, CDF has shown that the photon + jet mass distribution (Fig. 20) is also well described by the QCD expectation. This agreement can be used to place a limit on the production and decay of excited quarks, assuming the particular model of Baur et al. (Phys. Rev. D42(1990)815). Excited quarks with masses $80 < M_{Q^*} < 540$ GeV are excluded at the 95% confidence level (Fig. 21).

5.7 W + Jets Production and α_S

Understanding the QCD production of jets in association with $W^{\pm}$ bosons is of particular importance at the present time since this process gives rise to the dominant background in the search for the top quark. The LO QCD predictions have been shown to give a reasonable description of the jet multiplicity distribution in W events (Fig. 22). The fraction of W

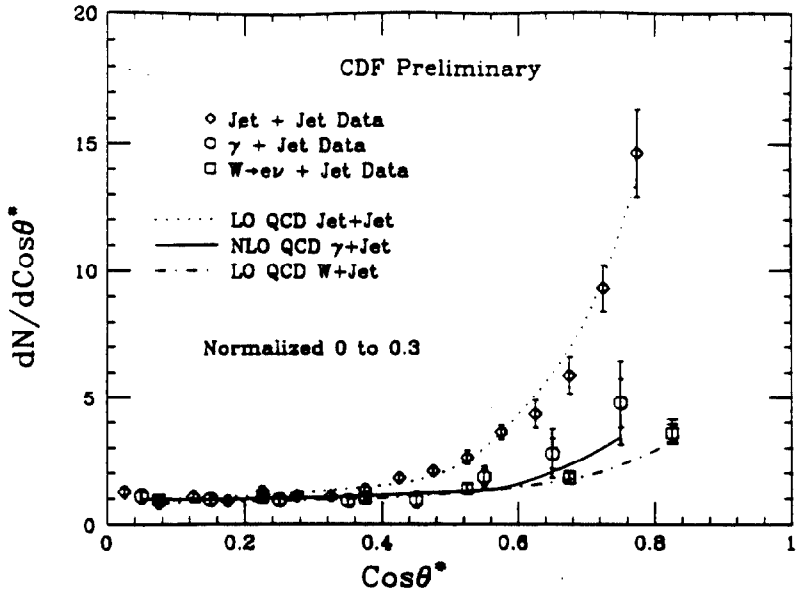

Figure 19: CDF two-jet, W+jet, and photon+jet angular distributions.

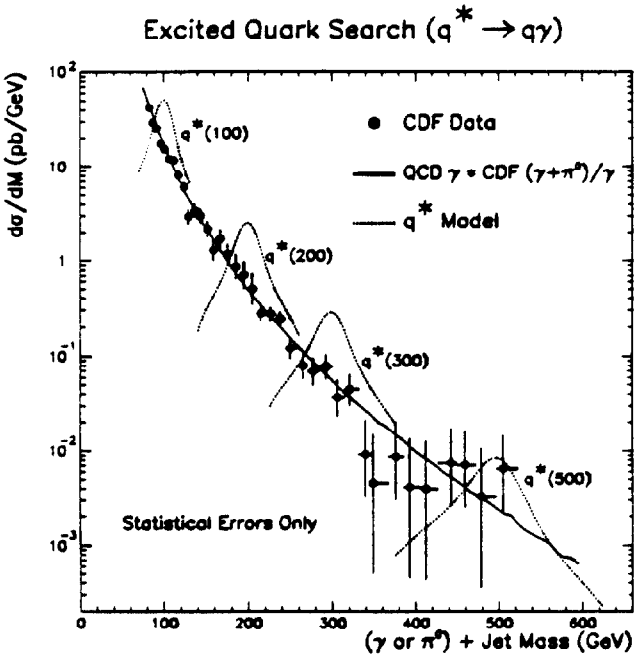

Figure 20: Photon candidate + Jet mass distribution compared with QCD predictions and expectations for an excited quark model (see text).

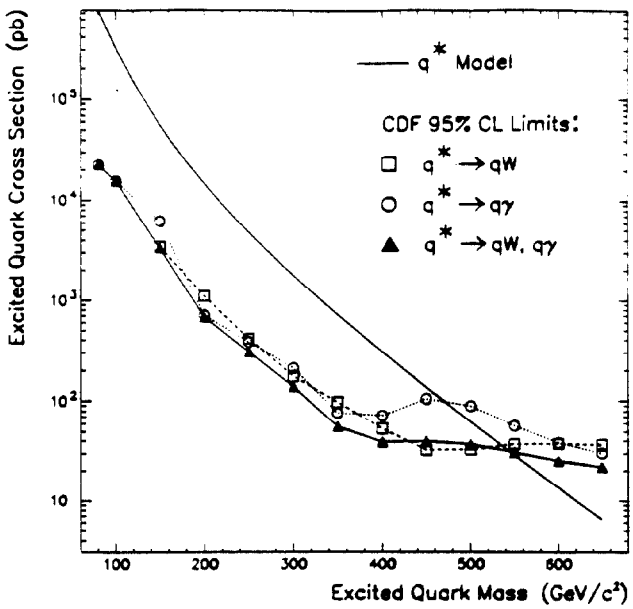

Figure 21: Cross-section limits on excited quark production.

bosons that are produced in association with jets is interesting in its own right since this fraction depends on α_s. The D0 collaboration have extracted a preliminary value of α_s from this fraction which, although not statistically competitive with LEP determinations of the strong coupling constant, never-the-less shows promise for the future (Fig. 23).

6 Testing the Electroweak Sector

The Fermilab proton-antiproton collider is the only machine currently operating that can produce real W bosons. Hence, electroweak tests at the collider have focussed on measuring the mass and width of the W, and the production of W bosons in association with other gauge bosons.

6.1 W Mass

At tree level the Standard Model has 3 parameters that determine the W and Z masses:

$$m_W = \frac{g}{2} \langle v \rangle \tag{13}$$

and

$$m_Z = \frac{g}{2}\sqrt{g^2 + g'^2} \langle v \rangle \tag{14}$$

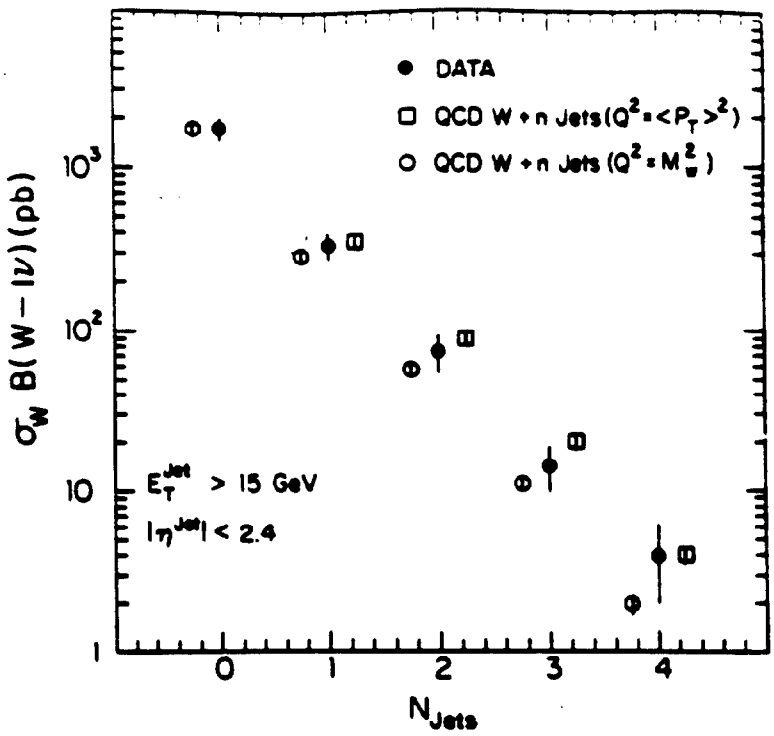

Figure 22: CDF measurement of W cross section times leptonic branching ratio for jet $E_T >$ 15 GeV shown as a function of jet multiplicity.

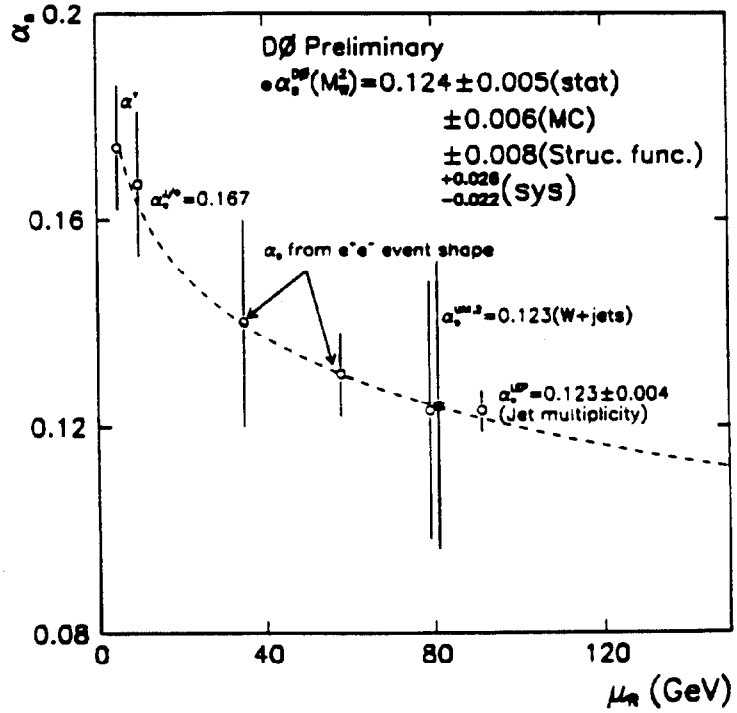

Figure 23: D0 measurement of α_s in W + jet events compared with world data.

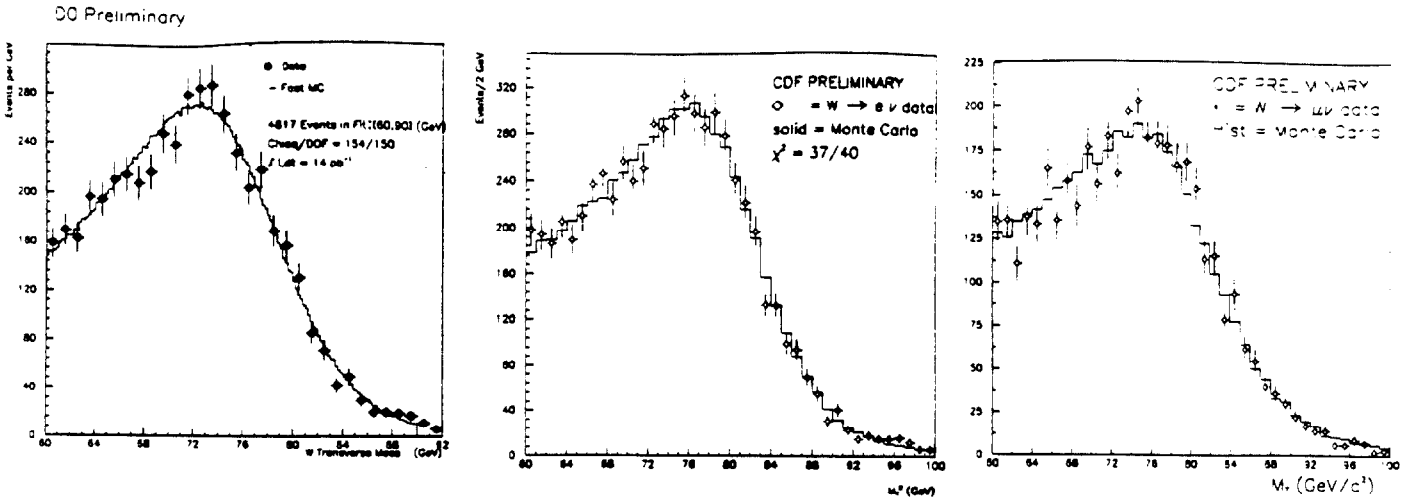

Figure 24: W transverse mass distributions for D0 electron events (left), CDF electron events (middle) and CDF muon events (right). Note that D0 plots from 60 to 92 and CDF plots from 60 to 100 GeV/c^2.

where $\langle v \rangle$, g and g' are respectively the vacuum expectation value of the Higgs field, the coupling of the SU(2)$_L$ isotriplet weak bosons to the left-handed weak currents, and the coupling the U(1) isosinglet B to the hypercharge current. Radiative corrections change these predictions for the W and Z masses. The top mass m_t enters quadratically through self-energy loop diagrams in which the W couples to a virtual $t\bar{b}$ pair or the Z couples to a virtual $t\bar{t}$ pair. These loop corrections increase with increasing top mass like m_t^2/m_W^2. An upper limit on m_t can be derived from a comparison of $\sin^2\theta_W$ extracted from the measured W and Z masses with $\sin^2\theta_W$ measured in low energy neutrino scattering. In addition, the Higgs mass m_H also contributes logarithmically to the W and Z masses. Thus, there are 5 electroweak parameters that dominate the observed W and Z masses and couplings: $\langle v \rangle$, g, g', m_t, and m_H. At present there are three electroweak parameters which are precisely measured: α, G_F, and m_Z. We therefore need precision measurements of two additional electroweak parameters: m_W, and m_t.

To determine the W mass, CDF is currently using a sample of 6510 $W \to e\nu$ decays and 4090 $W \to \mu\nu$ decays, and D0 is using a sample of 4817 $W \to e\nu$ decays. The momenta of the charged leptons is measured precisely using the CDF and D0 calorimeters and tracking systems. The energetic neutrinos do not deposit energy in the detectors. However their presence results in an apparent imbalance of transverse momenta in the W events (the so called $\not\!\!E_T$). The transverse components of the neutrinos are therefore identified with the measured $\not\!\!E_T$ vectors. Since the beam directions are blind spots for the collider detectors, the longitudinal component of the neutrino cannot be determined in this way. To overcome

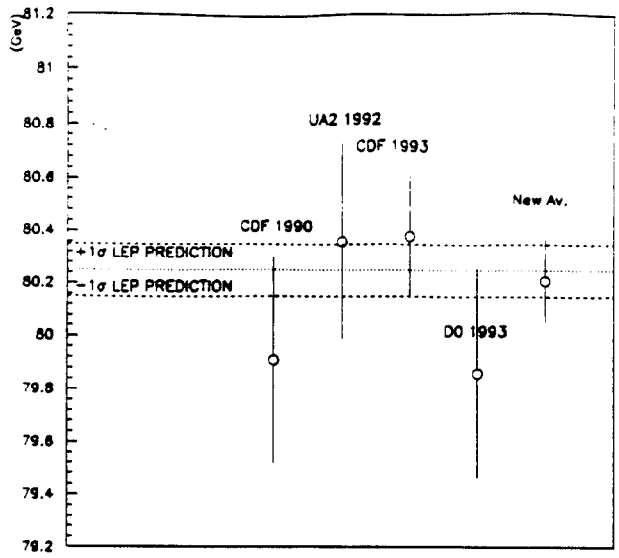

Figure 25: Summary of world W mass measurements.

this difficulty the W mass is determined by CDF and D0 by fitting the distribution of lepton-neutrino transverse mass ($m_T^{l\nu}$) measured in $W \to l\nu$ decays, where

$$m_T^{l\nu} = \sqrt{(E_T^e + E_T^\nu)^2 - (\vec{p}_T^{\,e} + \vec{p}_T^{\,\nu})^2} \tag{15}$$

The fitted CDF and D0 distributions are shown in Figure 24, and the results are summarized in Fig. 25. The latest preliminary results are:

$$m_W = 79.86 \pm 0.26\ GeV \quad (CDF\ Preliminary) \tag{16}$$

$$m_W = 80.38 \pm 0.23\ GeV \quad (D0\ Preliminary) \tag{17}$$

$$m_W = 80.23 \pm 0.18\ GeV \quad (World\ Average) \tag{18}$$

The quoted uncertainties, which include both systematics and the statistical uncertainties from the fits, are expected to decrease in the near future.

6.2 W Width

A measurement of the W width Γ_W is an important test of the standard model. Deviations from the standard model prediction for Γ_W might indicate additional W decay channels arising from physics beyond the standard model. The direct way of determining Γ_W is to

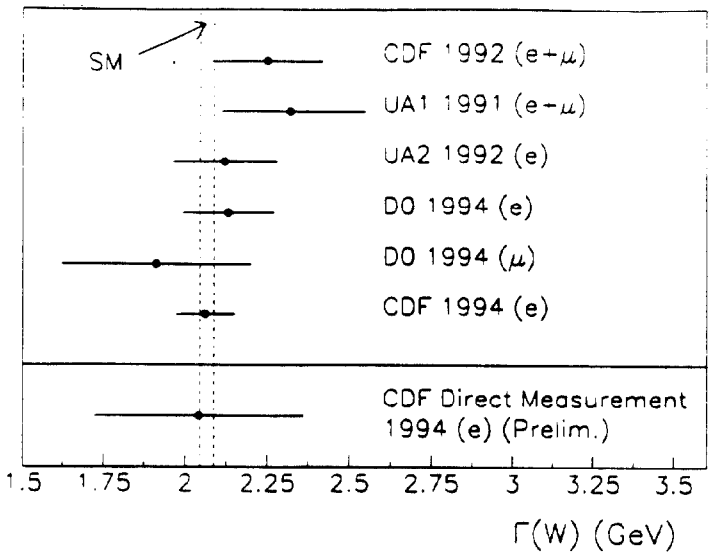

Figure 26: Summary of world W width measurements.

leave it as a free parameter in the W transverse mass fits. However, this method yields results with relatively poor precision. A more precise although less direct method has been developed based on the ratio R:

$$R = \frac{\sigma(W \to l\nu)}{\sigma(Z^0 \to l^+l^-)} = \frac{\sigma(\bar{p}p \to Z^0X)}{\sigma(\bar{p}p \to WX)} \frac{\Gamma(W \to l\nu)}{\Gamma(Z^0 \to l^+l^-)} \frac{\Gamma(Z^0)}{\Gamma(W)} \tag{19}$$

The ratio of production cross-sections has been calculated at NNLO. The ratio of leptonic partial widths is given by the standard model, and the total Z^0 width has been measured at LEP. Hence a measurement of R can be used to determine Γ_W. The CDF + D0 average value for R is:

$$R = 10.91 \pm 0.36 \; (\sqrt{s} = 1.8 \; TeV) \tag{20}$$

Taking $\Gamma(W \to l\nu) \; / \; \Gamma(Z \to l^+l^-) = 2.710 \pm 0.018$, gives:

$$B(W \to l\nu) = 0.1095 \pm 0.0037 \tag{21}$$

and

$$\Gamma_W = 2.061 \pm 0.069 \; GeV \tag{22}$$

The worlds measurements of Γ_W are therefore consistent with the standard model expectation of 2.067 ± 0.021 GeV (Fig. 26). If the top quark is sufficiently light to permit $W \to t\bar{b}$

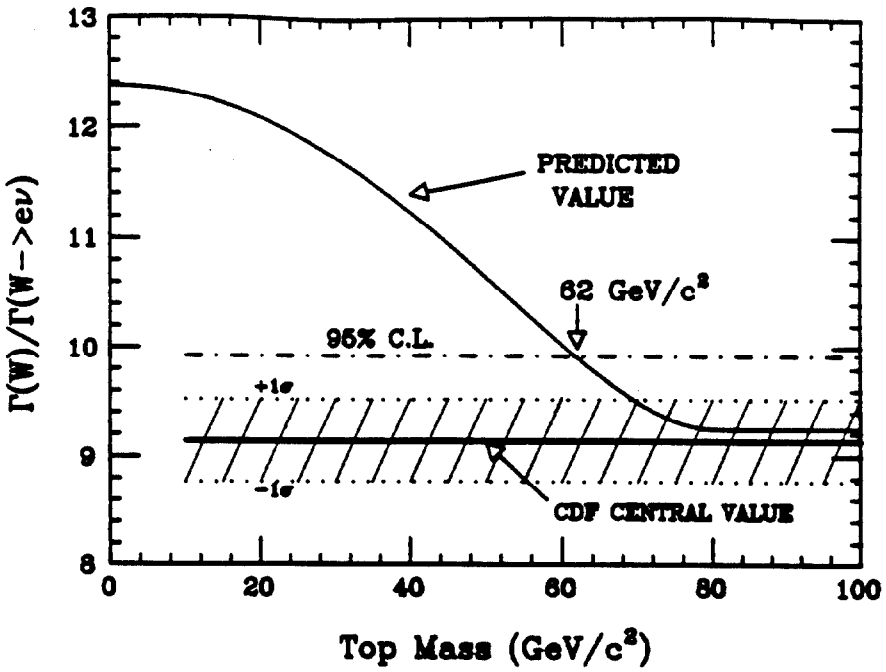

Figure 27: CDF determination of the W width.

decays then Γ_W will be sensitive to the m_t. The measured value of Γ_W is consistent with there being no contribution from the $t\bar{b}$ channel. The CDF measurement implies that $m_t >$ 62 GeV (Fig. 27).

6.3 The Three-Boson Coupling

The standard model couplings of gauge bosons to quarks and leptons are well tested. However gauge invariance in the standard model also requires the existence of trilinear couplings (WWγ and WWZ) between three electroweak gauge bosons. At the Fermilab proton-antiproton collider these couplings are expected to contribute to the production of events with two vector bosons in the final state (W^+W^-, $W^\pm Z^0$, or $W^\pm\gamma$). Measurements of the rate and properties of these diboson events therefore provide a test of the three-boson couplings. Let us begin with $W^\pm\gamma$ events. The standard model describes the coupling between W bosons and photons in terms of two CP-conserving coupling constants; κ and λ, where at tree level $\kappa = 1$ and $\lambda = 0$. These couplings are related to the W magnetic dipole and electric quadrupole moments, μ_W and Q_W :

$$\mu_W = \frac{e}{2m_W}(1 + \kappa + \lambda) \tag{23}$$

CDF	D0	Notes
$-2.3 < (\kappa - 1) < 2.2$	$-2.3 < (\kappa - 1) < 2.3$	$for\ \lambda = 0$
$-0.7 < \lambda < 0.7$	$-0.7 < \lambda < 0.7$	$for\ \kappa = 1$
$-2.3 < \tilde{\kappa} < 2.2$	$-2.3 < \tilde{\kappa} < 2.3$	$for\ \tilde{\lambda} = 0$
$-0.7 < \tilde{\lambda} < 0.7$	$-0.7 < \tilde{\lambda} < 0.7$	$for\ \tilde{\kappa} = 0$

Table 3: Limits on deviations of the $WW\gamma$ couplings from standard model expectations (95% C.L.) derived from CDF and D0 Wγ event measurements.

Moment	Result	Notes
Electric Quadrupole	$-6.0 < q^e_{Z_T} < 6.0$	$for\ q^m_{Z_T} = \delta_{Z_T} = g_{Z_T} = 0$
Magnetic Quadrupole	$-6.0 < q^m_{Z_T} < 6.0$	$for\ q^e_{Z_T} = \delta_{Z_T} = g_{Z_T} = 0$
Electric Dipole	$-1.1 < \delta_{Z_T} < 1.1$	$for\ q^e_{Z_T} = q^m_{Z_T} = g_{Z_T} = 0$
Magnetic Dipole	$-1.1 < g_{Z_T} < 1.1$	$for\ q^e_{Z_T} = q^m_{Z_T} = \delta_{Z_T} = 0$

Table 4: CDF Preliminary 95% C.L. limits on Z^0 dipole and quadrupole moments coming from the measured $Z\gamma$ cross-section.

$$Q_W = -\frac{e}{m_W^2}(\kappa - \lambda) \tag{24}$$

In a more general model there are also two CP-violating couplings $\tilde{\kappa}$ and $\tilde{\lambda}$ which are equal to zero in the standard model. Hence measured $W^{\pm}\gamma$ event rates enables determination of the couplings κ, λ, $\tilde{\kappa}$, and $\tilde{\lambda}$, or alternatively determination of μ_W and Q_W. Both CDF and D0 have measured $W^{\pm}\gamma$ event rates. CDF observes 25 candidate $W^{\pm}\gamma$ events with an estimated background of 8.7 ± 2.0 events. D0 observe 19 candidate $W^{\pm}\gamma$ events. Both observations are consistent with standard model expectations. The resulting limits on deviations from the expected three-boson couplings are essentially identical for the two experiments, and are summarized in Table 3.

We now turn our attention to the WWZ coupling which is expected to contribute to WW and WZ diboson production. The predicted production cross-sections for the WW and WZ final states are respectively 9.5 pb and 2.5 pb. Thus, with the present CDF and D0 integrated luminosites of a few times 10 pb^{-1}, afer selection cuts we would expect at most a few events. In the CDF WW and WZ searches the standard model expectations are 1.6 $WW \to l\nu\, l\nu$ events and 0.1 $WZ \to l\nu\, ll$ events. CDF sees no $WW \to l\nu\, l\nu$ candidates and one beautiful $WZ \to e\nu\, e^+e^-$ event. Within the very limited statistics these observations are consistent with the standard model expectations.

Finally, both CDF and D0 have searched for $Z\gamma$ events. In the standard model these arise only from the fermion-boson couplings since the $ZZ\gamma$ and $Z\gamma\gamma$ couplings are zero. In fact the coupling between Z bosons and photons can be described in terms of four CP-conserving and four CP-violating couplings, all of which are zero in the standard model. The eight couplings are related to the Z^0 electric dipole and quadrupole moments (δ_{Z_T} and $q^e_{Z_T}$), and the Z^0 magnetic dipole and quadrupole moments (g_{Z_T} and $q^m_{Z_T}$). CDF have measured the $Z\gamma$ cross-section to be 4.6 ± 1.7 $(stat) \pm 0.5$ (sys) pb, in good agreement with the standard model expectation of 4.8 ± 0.6 pb. D0 have also observed $Z\gamma$ events; $5.7^{+3.6}_{-1.6} \pm 0.1$ (sys) after background subtraction, which is in agreement with the standard model expectation for their analysis of 8.2 ± 0.6 $(sys) \pm 1.1$ $(luminosity)$ events. Thus it appears that the present data is in agreement with standard model predictions in which the $ZZ\gamma$ and $Z\gamma\gamma$ couplings are absent. The resulting limits on the Z^0 dipole and quadrupole moments are shown in Table 4.

7 The Top Quark

Prior to the current collider run the top quark was the only standard model quark that had not yet been observed. CDF limits on top quark production from the 1988-89 run had already excluded top quarks with a mass $m_t < 91$ GeV at 95% C.L. On the other hand, global fits to precision electroweak measurements yielded a predicted mass $m_t = 164^{+17+18}_{-16-20}$ GeV. By the end of the current collider run the CDF and D0 data samples should be sufficient to explore this mass range ... an exciting prospect. In addition to the excitement of discovery, there is the even more exciting possibility that by studying the production of the very heavy top quark we will learn something about the origin of quark masses. The predicted cross-section for $\bar{p}p \to t\bar{t} + X$ in the relevant top quark mass range is only of order 10 pb. We therefore expect something like one $t\bar{t}$ event in every 10^{10} collisions. Noting that the CDF and D0 run 1a data samples correspond to an integrated luminosity of about 20 pb^{-1}, we would expect the experiments to have recorded no more than a few $t\bar{t}$ events so far. Top quark production and decay is shown schematically in Fig. 28, and final state branching ratios are listed in Table 5. About 5% of the time both W bosons decay to $e\nu$ or $\mu\nu$, which results in two isolated oppositely charged leptons in the final state (the DILEPTON mode). This provides a clean signal topology with low background rates, but unfortunately also a low signal rate. About 30% of the time one W decays to $e\nu$ or $\mu\nu$, and the other W decays to a $q\overline{q'}$ pair (the

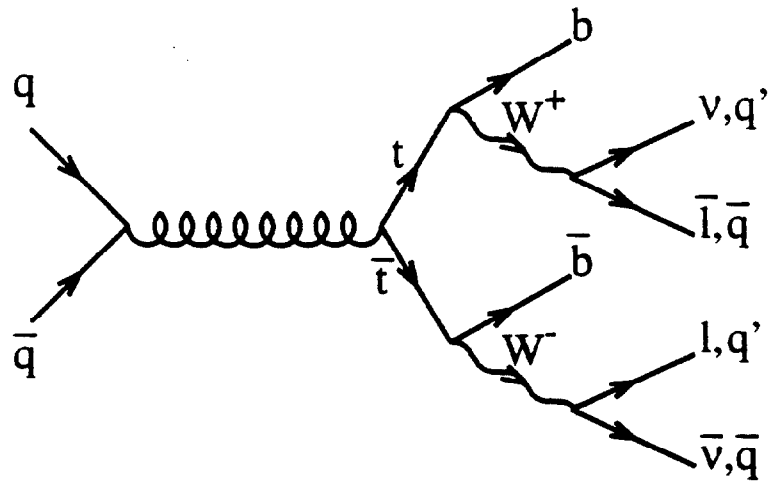

Figure 28: Tree level top quark production by $q\bar{q}$ annihilation followed by the Standard Model top quark decay chain.

LEPTON + JETS mode), which has a higher rate, but larger backgrounds.

7.1 The CDF Dilepton Search

The CDF dilepton search is designed to look for $t\bar{t}$ events in which both the t and $\bar{t}$ have decayed semileptonically. In these events we would expect two oppositely charged leptons (e^+e^-, $\mu^+\mu^-$, or $e^\pm\mu^\mp$), two b-quark jets, and $\not\!\!E_T$ from the energetic neutrinos. The CDF selection requires two oppositely charged leptons (e or μ) with $p_T > 20$ GeV, two jets with $E_T > 10$ GeV and $|\eta| < 2.4$, and $\not\!\!E_T > 25$ GeV. At least one lepton must be central ($|\eta| < 1$) and isolated. To remove Z^0 decays, lepton pairs with mass $75 < m_{l^+l^-} < 105$ GeV are rejected. Finally, to remove $Z^0 \to \tau^+\tau^-$ decays, the event is rejected if the $\not\!\!E_T < 50$ GeV and the azimuthal angle between the $\not\!\!E_T$ direction and the nearest jet ($\Delta\phi_{\nu J}$) is less than 20°. A feeling for the efficiency of these requirements can be obtained by looking at Fig. 29 which shows $t\bar{t}$ ISAJET Monte Carlo simulated distributions for the main quantities used in the selection. The calculated selection efficiency depends upon the top mass, and rises from 0.49 ± 0.07 for $m_t = 120$ GeV to 0.86 ± 0.07 for $m_t = 180$ GeV, where the quoted numbers include the branching ratios. Figure 30 shows the distribution of ee, eμ, and $\mu\mu$ events, and $t\bar{t}$ ISAJET Monte Carlo events in the ($\Delta\phi_{\nu J}$, $\not\!\!E_T$) plane before the $\not\!\!E_T$ and $\Delta\phi_{\nu J}$ cuts have been applied. There are two eμ events which pass the selection requirements, and no ee or $\mu\mu$ events. The expected backgrounds come from W^+W^- production (0.16 ± 0.06

Decay mode	Branching ratio
$t\bar{t} \longrightarrow (q\bar{q}'b)(q\bar{q}'\bar{b})$	36/81
$t\bar{t} \longrightarrow (q\bar{q}'b)(e\nu\bar{b})$	12/81
$t\bar{t} \longrightarrow (q\bar{q}'b)(\mu\nu\bar{b})$	12/81
$t\bar{t} \longrightarrow (q\bar{q}'b)(\tau\nu\bar{b})$	12/81
$t\bar{t} \longrightarrow (e\nu b)(\mu\nu\bar{b})$	2/81
$t\bar{t} \longrightarrow (e\nu b)(\tau\nu\bar{b})$	2/81
$t\bar{t} \longrightarrow (\mu\nu b)(\tau\nu\bar{b})$	2/81
$t\bar{t} \longrightarrow (e\nu b)(e\nu\bar{b})$	1/81
$t\bar{t} \longrightarrow (\mu\nu b)(\mu\nu\bar{b})$	1/81
$t\bar{t} \longrightarrow (\tau\nu b)(\tau\nu\bar{b})$	1/81

Table 5: Decay modes for a $t\bar{t}$ pair and their approximate branching ratios (to lowest order) assuming charged-current decays. The symbol q stands for a light quark.

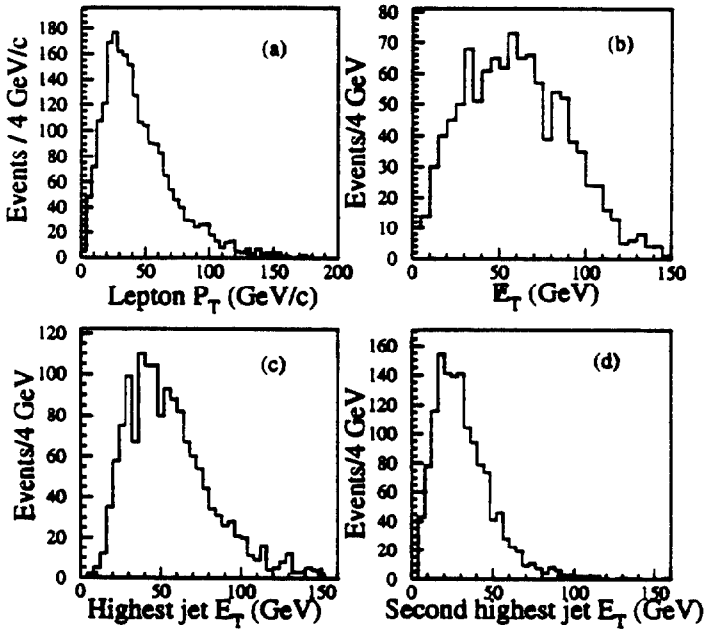

Figure 29: Monte Carlo distributions for m_t=160 GeV/c^2. a) Lepton p_T spectrum from $t \rightarrow W \rightarrow l$. b) $\not\!\!E_T$ for events with two leptons with $p_T > 20$ GeV/c. c) Leading-jet E_T for dilepton events. d) Next-to-leading jet E_T for dilepton events.

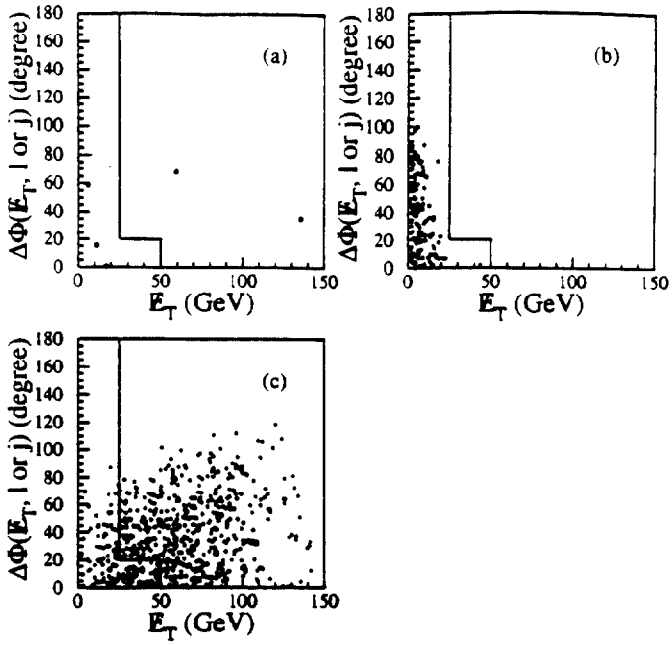

Figure 30: Distributions of the azimuthal angle between the $\not\!\!E_T$ and closest lepton or jet versus the $\not\!\!E_T$. a) $e\mu$ data. b) Dielectron and dimuon data after the invariant mass cut. c) Monte Carlo events for M_{top}=160 GeV/c^2 (unnormalized).

events), $Z \rightarrow \tau^+\tau^-$ decays (0.13 ± 0.04 events), $b\bar{b}$ and $c\bar{c}$ production (0.10 ± 0.06 events), fake leptons (0.07 ± 0.05 events), and Drell-Yan production ($0.10^{+0.25}_{-0.13}$ events). Thus CDF observes 2 dilepton events with a total predicted background of $0.56^{+0.25}_{-0.13}$ events.

7.2 The CDF Lepton + Jets Search

The CDF lepton + jets search is designed to look for $t\bar{t}$ events in which one member of the $t\bar{t}$ pair decayed semileptonically and the other member decayed hadronically. In these events we would expect one charged lepton (e or μ) and large $\not\!\!E_T$ from the $W \rightarrow l\nu$ decay, plus two b-quark jets, and two light-quark jets. The CDF lepton + jets selection requires an isolated e or μ with $p_T > 20$ GeV and $|\eta| < 1$, $\not\!\!E_T > 20$ GeV, and at least 3 jets with $E_T > 15$ GeV and $|\eta| < 2$. To remove Z^0 decays, if there is a second lepton in the event with lepton pair mass $75 < m_{l^+l^-} < 105$ GeV then the event is rejected. This selection yields 52 $W+ \geq 3$ jet candidates, of which 9 events have more than 3 jets. To further suppress the backgrounds, particularly the background from QCD $W+ \geq 3$ jet production, CDF next requires that at least one jet is tagged as a b-quark jet. There are two complementary methods used to tag b-quark jets, which are described in the following paragraphs.

The first CDF b-tagging method exploits the long B meson lifetime which results in B

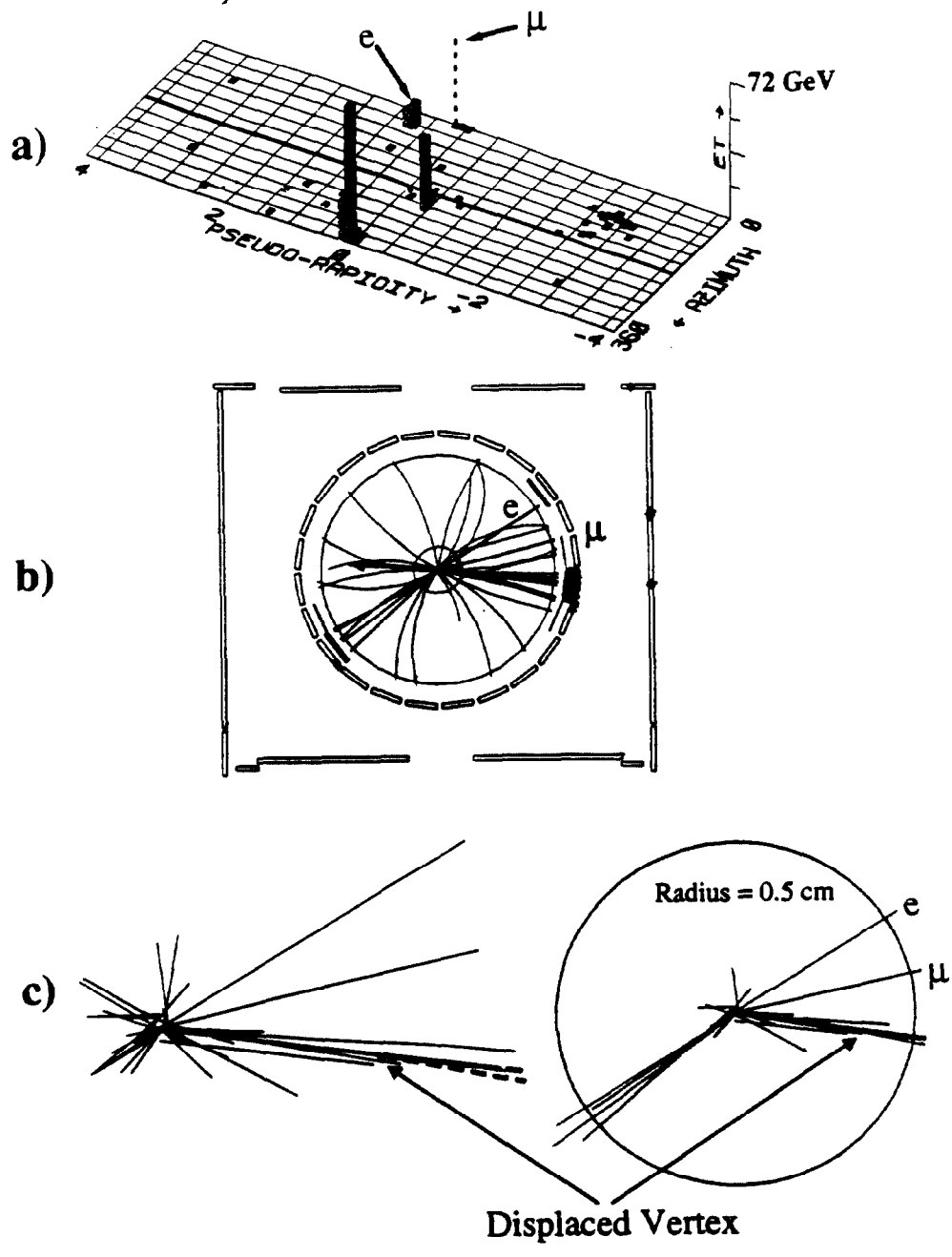

Figure 31: Event display for one of the $e\mu$ events; (a) displays the Lego plot, (b) shows the reconstructed tracks and muon hits in the $r-\phi$ plane, and (c) shows the reconstructed SVX tracks. The track lengths in the SVX display are proportional to their p_T.

mesons travelling a measurable distance from the interaction vertex before decaying. The CDF Silicon Vertex Detector is used to search for b-quark decay vertices that tag one of the jets in the event as a b-quark jet. This method has enabled CDF to make a great variety of b-quark physics measurements. Figure 32 shows as an example a $B_s \rightarrow J/\psi\ K^*$ candidate event in which the $K^+\pi^-\mu^+\mu^-$ system is clearly seen in the SVX to be displaced from the primary vertex. Furthermore, opposite the $B \rightarrow J/\psi$ decay there is a second jet which is also clearly displaced from the primary vertex, the $\bar{b}$ jet. The high quality of the SVX data has enabled the exponential decay length distribution to be measured and the B lifetime to be extracted. The measured lifetime, $1.46 \pm 0.06\ (stat) \pm 0.06\ (sys)$ ps, is in good agreement with the worlds data (Fig. 33). Thus the SVX b-quark tagging method is well understood. The overall efficiency of the CDF $W+ \geq 3$ jet selection with an SVX tag has been calculated using the ISAJET $t\bar{t}$ Monte Carlo program. The calculated efficiency, including branching ratios, depends on top quark mass and rises from $1.0 \pm 0.3\%$ for $m_t = 120$ GeV to $1.8 \pm 0.6\%$ for $m_t = 180$ GeV. CDF finds 6 SVX b-quark tags in the 52 $W+ \geq 3$ jet events. The expected background arises from $Wb\bar{b}$, $Wc\bar{c}$, and mistags (1.99 ± 0.26 events), Wc production (0.14 ± 0.07 events), $Z \rightarrow \tau^+\tau^-$ decays plus WW and WZ production (0.08 ± 0.04 events), and non-W related background which includes $b\bar{b}$ production (0.09 ± 0.09 events). Thus CDF observes 6 $W+ \geq 3$ jet events with SVX tags where the total background is expected to be 2.30 ± 0.29 events.

The second CDF b-tagging method searches for additional leptons in the event arising from semileptonic decays of the b-quarks or their daughter c-quarks. These leptons typically have lower p_T than leptons arising from W decays, hence these b-quark tags are refered to as soft lepton tags. The CDF soft lepton tag search requires that the lepton (e or μ) has $p_T > 2$ GeV. To avoid double counting, events which pass the diplepton selection are not considered. The calculated efficiency for $t\bar{t}$ events to pass the $W+ \geq 3$ jet selection and have a soft lepton tag, including branching ratios, rises from $0.84 \pm 0.17\%$ for $m_t = 120$ GeV to $1.3 \pm 0.2\%$ for $m_t = 180$ GeV. In the 52 $W+ \geq 3$ jet events CDF finds 7 events with a soft lepton tag, of which 3 events also have an SVX b-quark tag. The expected background arises from $Wb\bar{b}$, $Wc\bar{c}$, and fakes (2.70 ± 0.27 events), $b\bar{b}$ production (0.05 ± 0.03 events), diboson production (0.04 ± 0.03 events), $Z \rightarrow \tau^+\tau^-$ decays (0.14 ± 0.06 events), Drell-Yan production (0.05 ± 0.05 events), and Wc production (0.08 ± 0.03 events). Thus CDF observes 7 $W+ \geq 3$ jet events with a soft lepton tag where the calculated background is 3.1 ± 0.3 events.

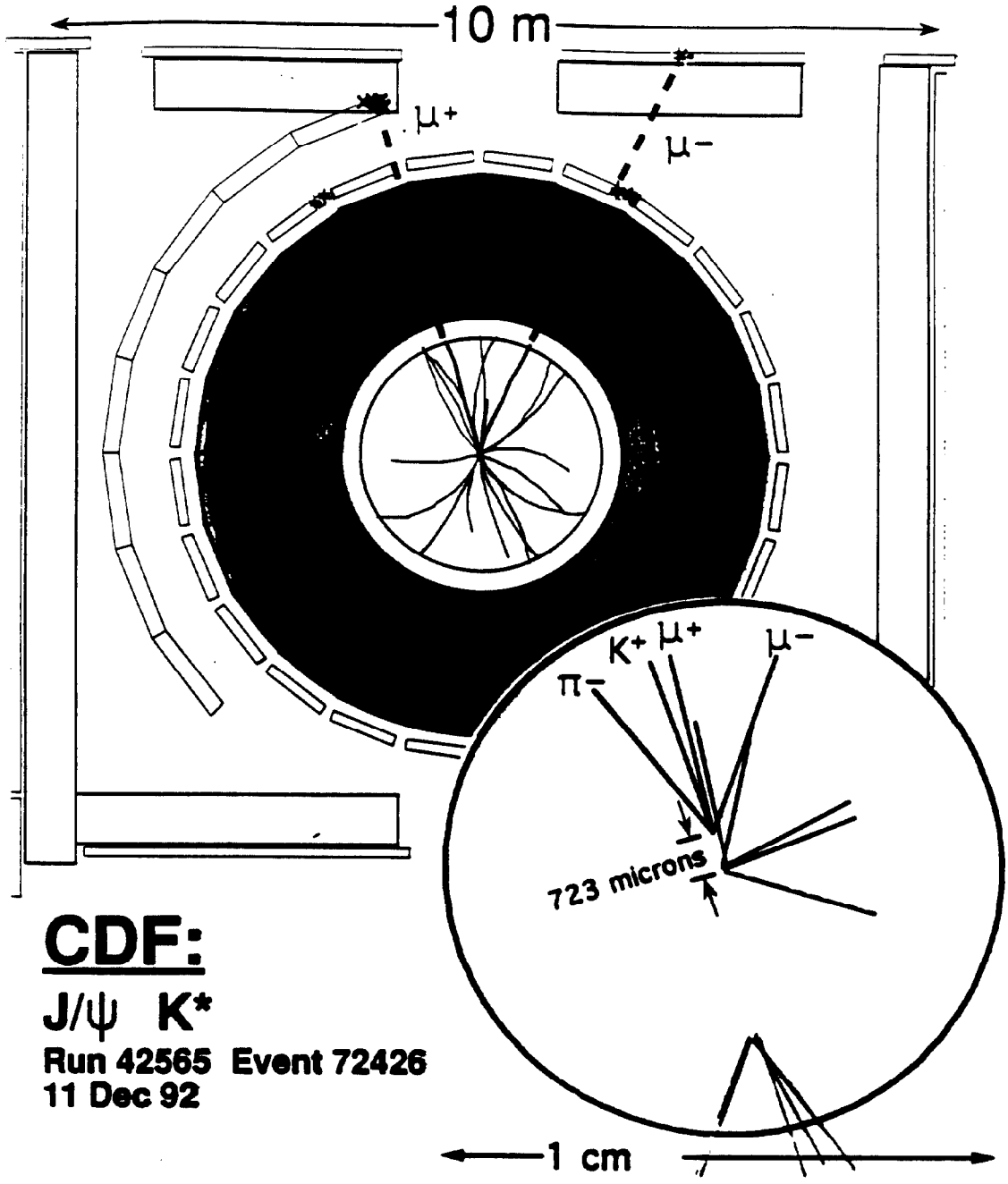

Figure 32: Example of a $B_S \rightarrow J/\psi\ K^*$ decay observed in the CDF detector.

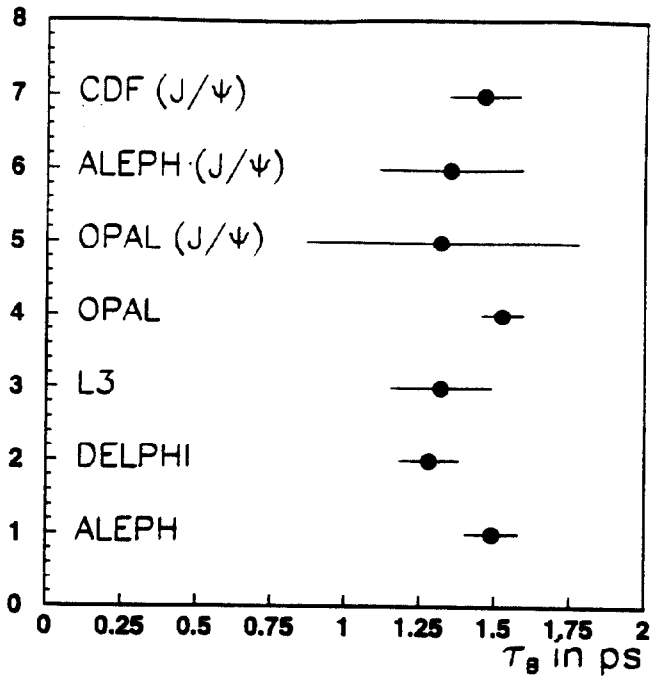

Figure 33: Comparison of CDF inclusive B meson lifetime measurement with the worlds data.

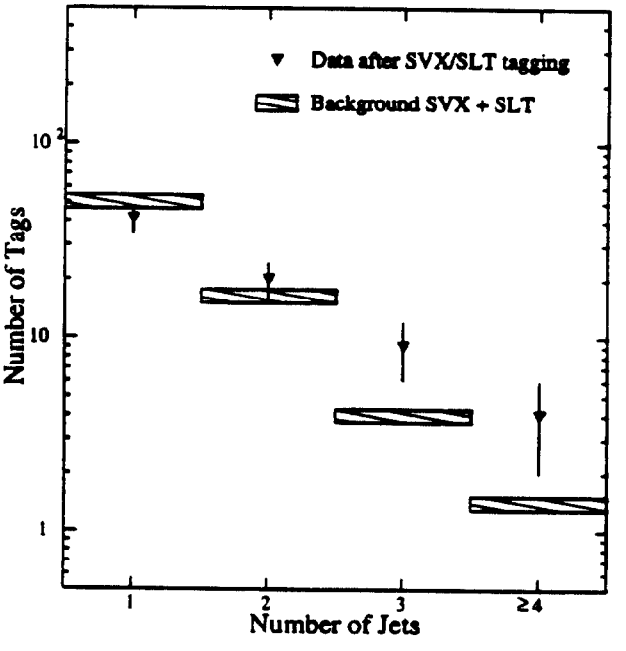

Figure 34: The sum of CDF SVX and soft lepton tags observed in W + jets data compared with background estimates. The three-jet and four-jet bins are the $t\bar{t}$ signal region.

Search Category	Expect m=160	Background	Observed
D0 SEARCHES			
Dilepton	0.83	0.98	1
Kinematic	2.8	1.6	3
Soft lepton tag	1.6	2.1	3
D0 SUM	5.4 ± 0.9	4.7 ± 1.0	7
CDF SEARCHES			
Dilepton	1.3	0.56	2
Soft lepton tag	1.9	3.1	7
Silicon vertex tag	2.7	2.3	6
CDF SUM	5.9	5.9	15 (12 events)

Table 6: D0 and CDF Top Searches at a Glance.

The CDF lepton + jets search results are summarized in Fig. 34. There are 10 $W+ \geq 3$ jet events with a b tag (SVX or soft lepton) of which 3 events are tagged by both methods.

7.3 CDF Results and Their Interpretation

The CDF top search results are summarized in Table 6. The calculated probability that the backgrounds have fluctuated upwards to result in the observed numbers of events is 0.25%. Individual events can be kinematically fitted for m_t. The result of fitting a subsample of 7 events which are tagged and have ≥ 4 observed jets (so that both b jets and both light quark jets have been observed), is shown in Fig. 35. The fitted mass:

$$m_t = 174 \pm 10\ (stat)\ ^{+13}_{-12}\ (sys)\ \ GeV \tag{25}$$

For this mass, the measured cross-section:

$$\sigma_{t\bar{t}} = 13.9^{+6.1}_{-4.8}\ pb \tag{26}$$

which is a little higher than, but consistent with, the predicted cross-section for $m_t = 174$ GeV (Fig. 36). The CDF collaboration conclude that these results are evidence for, but given the limited statistics do not firmly establish the existence of, $t\bar{t}$ production. To confirm this observation and improve the measurement of the top quark properties, more data is needed. By the end of run 1 CDF expect to quadruple their data sample, and hopefully firmly establish the discovery of the top quark.

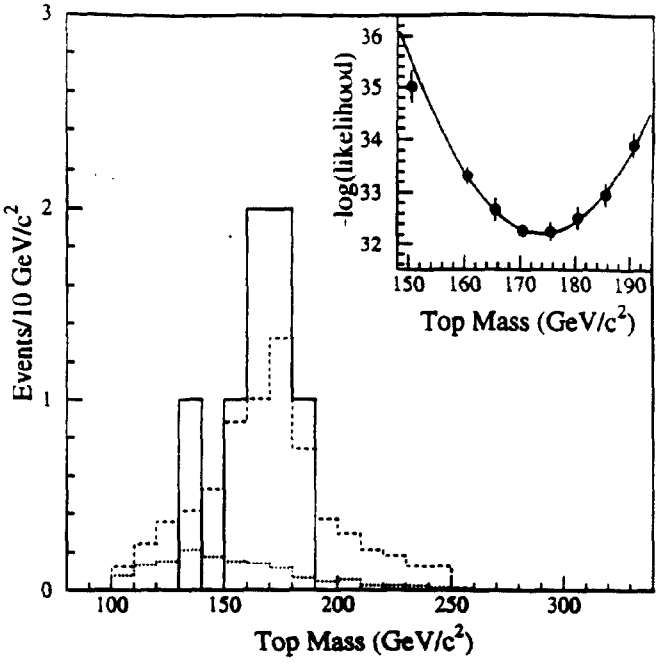

Figure 35: CDF top mass distribution (solid histogram) compared with the W + jets background prediction (dots) and the predicted signal+background distribution normalized to the data for $m_t = 175$ GeV (dashed). The inset shows the likelihood fit results.

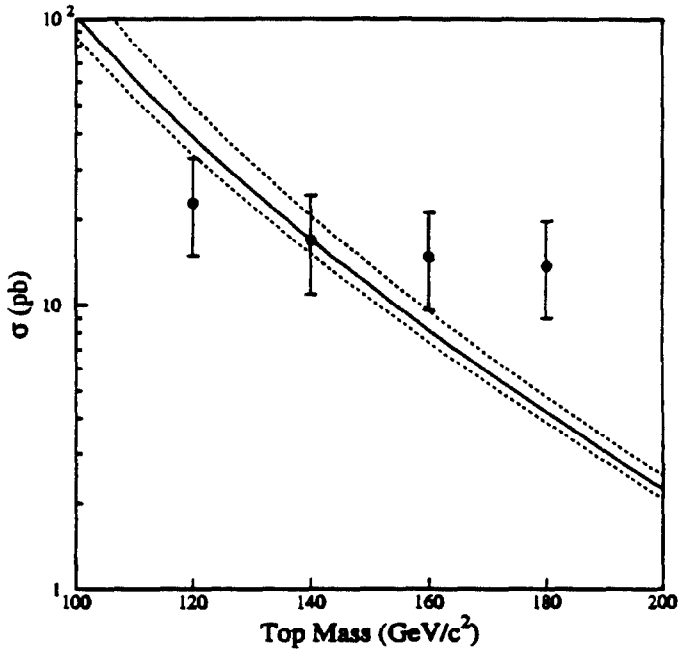

Figure 36: Measured $t\bar{t}$ cross section (points) compared with theory (E. Laenen, J. Smith, and W.L. Van Neerven, Phys. Lett 321B,254(1994)) shown as a function of top quark mass.

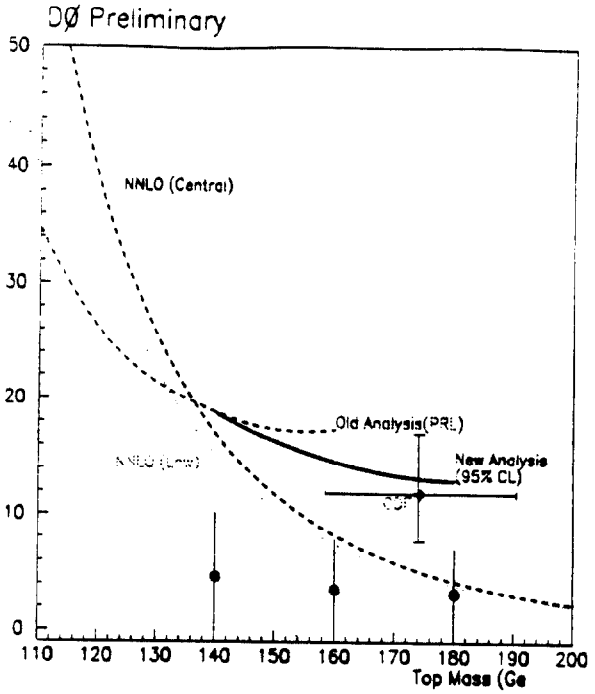

Figure 37: D0 $t\bar{t}$ cross section (pb), updated since the limit publication, showing the CDF measurement scaled to the D0 normalization, and the nominal and lowest NNLO predictions.

7.4 Consistency of the D0 Search Results

The D0 collaboration have also searched for $t\bar{t}$ events in the dilepton and soft lepton tag modes, and by a kinematic method. Since D0 has no SVX they are unable to use the powerful vertex tagging method. The D0 results are shown in Table 6 and Fig. 37. D0 do not find significant evidence for $t\bar{t}$ production. Whilst CDF has a top mass measurement of $m_t = 174 \pm 17$ GeV, D0 has a lower limit of 131 GeV (95% C.L.). Although D0 does not confirm the CDF result, the CDF and D0 results are consistent with one another.

8 Summary

These lecture notes have discussed a selection of current physics topics from the great variety of results obtained by the CDF and D0 experiments at the Fermilab Tevatron proton-antiproton collider. The immediate future looks very promising. In the next year CDF and D0 expect to quadrupule their datasets. This will result in significant improvements to the QCD and electroweak measurements described in this document, and will hopefully result in the confirmation of the CDF top quark discovery. In the longer term, further collider

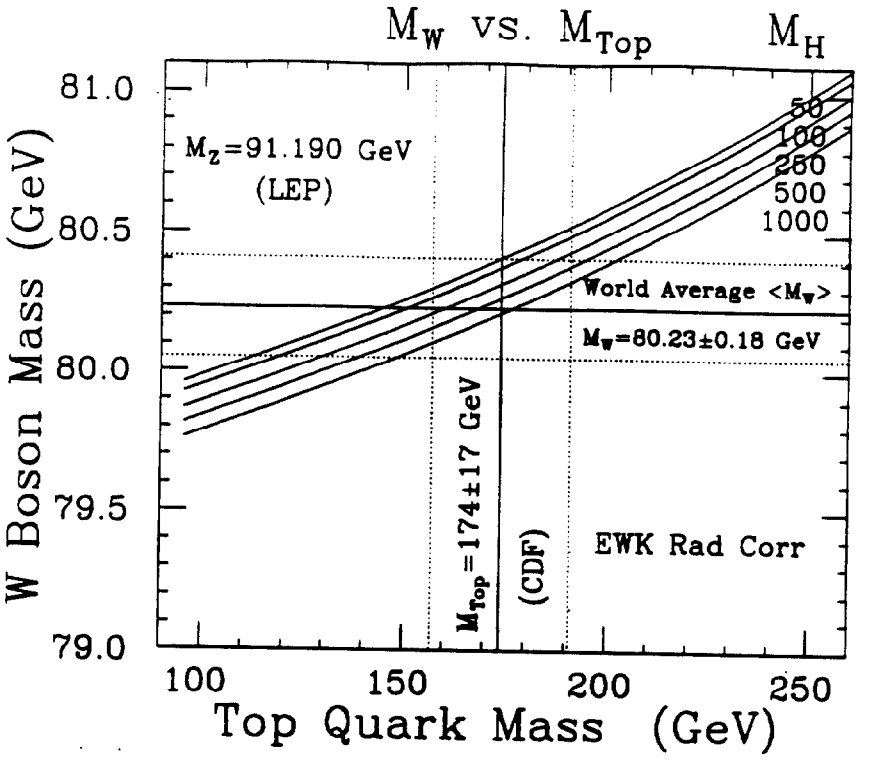

Figure 38: Top mass versus W mass.

running is expected to produce data samples of order 1000 pb^{-1}, with improved CDF and D0 detectors. This will permit more extensive top quark studies, greatly improved measurements of the triboson couplings, improved QCD and W mass measurements, and although not discussed in these notes, substantially extended b-quark physics results that may perhaps result in measurements of CP violation in the $B - \overline{B}$ system. Returning to the present, a fitting point to end these lectures is with Fig. 38 which shows the CDF plot of the measured W mass versus the measured top quark mass, compared with standard model predictions using the LEP measured Z mass, and shown as a function of the unknown Higgs boson mass.

Acknowledgements

I would like to thank the orginazers for inviting me to the BCSPIN school, and the Fermilab Accelerator, Research, and Computing Divisions, and the Fermilab Physics and Technical Support Sections for their vital contributions to the Collider program. I also acknowledge my many experimental CDF and D0 colleagues for the results discussed in these notes, and for the information and plots they have given me for these lectures.